Monthly Notices
of the
ROYAL ASTRONOMICAL SOCIETY

MNRAS **513,** 807–821 (2022)
Advance Access publication 2022 March 22

https://doi.org/10.1093/mnras/stac771

Gas-phase metallicity determinations in nearby AGNs with SDSS-IV MaNGA: evidence of metal-poor accretion

Janaína C. do Nascimento,[1,2]★ Oli L. Dors,[1]★ Thaisa Storchi-Bergmann,[2,3] Nícolas D. Mallmann,[2,3] Rogério Riffel,[2,3] Gabriele S. Ilha,[2,4] Rogemar A. Riffel,[2,4] Sandro B. Rembold,[2,4] Alice Deconto-Machado,[2,4] Luiz N. da Costa[2,5] and Mark Armah[3,5]

[1]*Universidade do Vale do Paraíba. Av. Shishima Hifumi, 2911, CEP: 12244-000 São José dos Campos, SP, Brazil*
[2]*Departamento de Física, CCNE, Universidade Federal de Santa Maria, 97105-900 Santa Maria, RS, Brazil*
[3]*Laboratório Interinstitucional de e-Astronomia – LIneA, Rua General José Cristino 77, Rio de Janeiro, RJ – 20921-400, Brazil*
[4]*Departamento de Astronomia, IF, Universidade Federal do Rio Grande do Sul, CP 15051, 91501-970 Porto Alegre, RS, Brazil*
[5]*Observatório Nacional, Rua General José Cristino, 77, Rio de Janeiro, RJ 20921-400, Brazil*

Accepted 2022 March 14. Received 2022 March 10; in original form 2021 September 3

ABSTRACT

We derive the metallicity (traced by the O/H abundance) of the narrow-line region (NLR) of 108 Seyfert galaxies as well as radial metallicity gradients along their galaxy discs and of these of a matched control sample of no active galaxies. In view of that, observational data from the SDSS-IV MaNGA survey and strong emission-line calibrations taken from the literature were considered. The metallicity obtained for the NLRs was compared to the value derived from the extrapolation of the radial oxygen abundance gradient, obtained from H II region estimates along the galaxy disc, to the central part of the host galaxies. We find that, for most of the objects ($\sim$ 80 per cent), the NLR metallicity is lower than the extrapolated value, with the average difference ($\langle D \rangle$) between these estimates ranging from 0.16 to 0.30 dex. We suggest that $\langle D \rangle$ is due to the accretion of metal-poor gas to the AGN that feeds the nuclear supermassive black hole (SMBH), which is drawn from a reservoir molecular and/or neutral hydrogen around the SMBH. Additionally, we look for correlations between D and the electron density (N_e), [O III]λ5007, and H α luminosities, extinction coefficient (A_V) of the NLRs, as well as the stellar mass (M_*) of the host galaxies. Evidence of an inverse correlation between the D and the parameters N_e, M_*, and A_v was found.

Key words: galaxies: abundances – galaxies: active – galaxies: evolution.

1 INTRODUCTION

Emission-line intensities present in the optical spectra of active galactic nuclei (AGNs) and star-forming regions (SFs) are essential to estimate the physical properties of the gas phase, such as metallicity, chemical abundances of heavy elements (e.g. O, N, S), electron temperature, and electron density of these objects. In particular, due to their high luminosity and prominent emission lines, AGNs play a key role in studies of the chemical evolution of galaxies along the Hubble time.

Oxygen abundance is usually used to estimate gas-phase metallicity of SFs (e.g. Kennicutt, Bresolin & Garnett 2003; Hagele et al. 2008; Yates, Kauffmann & Guo 2012) and of AGNs (e.g. Storchi-Bergmann et al. 1998; Dors et al. 2015, 2020b; Revalski et al. 2018; Flury & Moran 2020; Dors 2021). This is due to the oxygen is the third most abundant element after hydrogen and helium and it presents prominent optical emission lines ([O II]λ3726, λ3729, [O III]λ5007) of its most abundant ions (O^+, O^{2+}) measured in most part of the spectra with high signal-to-noise ratio. In fact, Skillman & Kennicutt (1993) and Dors et al. (2020b) found that the ion abundances with ionization stage higher O^{2+} do not exceed $\sim$ 5 per cent and $\sim$ 20 per cent of the total O/H abundance in SFs and AGNs, respectively. Therefore, such as in Krabbe et al. (2021), hereafter we use metallicity (Z) and oxygen abundance (in units of 12 + log(O/H)) interchangeably.

The metallicity has been estimated preferably by comparisons between observational emission-line ratios (e.g. [O II](λ3726+λ3729)/H β, [O III]λ5007/H β, [N II]λ6584/H α) with those predicted by photoionization models. One of the first Z determinations in AGNs was carried out by Ferland & Netzer (1983), who compared observed and model predicted optical emission-line ratios of low-ionization nuclear emission-line regions (LINERs) and Seyferts using the CLOUDY code (for the updated version, see Ferland et al. 2017). These authors found that the observed emission-line ratios were well reproduced by photoionization models with metallicity in the range $0.1 \lesssim (Z/Z_\odot) \lesssim 1.0$. After this pioneering work, several studies have been performed with the goal to estimate Z in AGNs located at low (e.g. Stasińska 1984; Ferland & Osterbrock 1986; Storchi-Bergmann et al. 1998; Groves, Heckman & Kauffman 2006; Feltre, Charlot & Gutkin 2016; Castro et al. 2017; Pérez-Montero et al. 2019; Carvalho et al. 2020) and high redshifts (e.g. e.g. Nagao, Maiolino & Marconi 2006; Matsuoka et al. 2009, 2018; Dors et al. 2018, 2019; Nakajima et al. 2018; Mignoli et al. 2019; Guo et al. 2020; Ji et al. 2020) by using photoionization models. Particularly, Storchi-Bergmann et al. (1998)

★ E-mail: jananasci02@gmail.com (JCN); dorsjunior@gmail.com (OLD)

proposed the first theoretical calibrations between strong optical emission-line ratios and metallicity, thus allowing estimations of Z in large samples of AGNs and the development of new calibrations (e.g. Dors et al. 2014, 2019; Castro et al. 2017; Carvalho et al. 2020; Dors 2021). Storchi-Bergmann et al. (1998) found that the Z-values of seven Seyfert 2 nuclei, derived from their calibrations, are in agreement (within an uncertainty of ∼0.2 dex) with those inferred from extrapolation of the oxygen abundance gradient to central parts of the hosting spiral galaxy. Thereafter, Dors et al. (2015) performed similar analysis but for a larger sample of AGNs (12 Seyfert 2) and star-forming nuclei (33 objects). Dors et al. (2015) found that direct central oxygen abundances (i.e. estimates based on emission-line ratios from the nuclei) in some high-metallicity galaxies tend to be lower than the extrapolated abundances.

The existence of lower oxygen abundances in the narrow-line region (NLR) of AGNs compared to the extrapolated value of abundance gradients is very important in chemical evolution studies of galaxies, since it indicates that the nuclear region could have distinct chemical evolution as compared to the disc. This discrepancy can be due to the following physical processes:

(i) Spiral galaxies in the local universe can be accreting metal-poor gas from the outskirts of the disc on to the centres, a process more common at very high redshift (e.g. Cresci et al. 2015; Gillman et al. 2021). However, cases at low redshift have also been reported in dwarf galaxies, e.g. in NGC 2915 (Werk et al. 2010) and NGC 4449 (Kumari, James & Irwin 2017).

(ii) The gas phase of AGNs can have a distinct depletion of oxygen on to dust grains (e.g. Sternberg, Genzel & Tacconi 1994; Usero et al. 2004) in comparison to the one in disc H II regions (of the order of 0.1 dex; e.g. Esteban et al. 1998; Meyer, Jura & Cardelli 1998; Izotov et al. 2006; Jenkins 2009; Whittet 2010).

(iii) There is metal-poor inflow of gas that can be originated from the capture of low mass companions to the nuclear region that ends up feeding the supermassive black hole (SMBH; e.g. Storchi-Bergmann et al. 2007).

To investigate which of these processes are acting in AGNs it is necessary to estimate the metallicity in the entire galaxy, i.e. to consider estimates along the disc and in the nuclear region. Sánchez et al. (2014), by using observational data of galaxies ($0.003 \lesssim z \lesssim 0.02$) selected by the Calar Alto Legacy Integral Field Area (CALIFA) survey (Sánchez et al. 2012), derived the oxygen gradients in about 300 spiral galaxies. However, the analysis carried out by Sánchez et al. (2014) was mainly based on galaxies containing star-forming nuclei. Another example is the CHAOS survey (Berg et al. 2015; Croxall et al. 2015, 2016; Berg et al. 2020; Skillman et al. 2020; Rogers et al. 2021), which has the selection criterion to observe only galaxies with star-forming nuclei. However, surveys such as Sydney Australian Astronomical Observatory Multi-object Integral Field Spectrograph (SAMI; Croom, Lawrence & Bland-Hawthorn 2012), although not dedicated to chemical evolution studies has provided valuable information on the nature of AGNs and their host galaxies (e.g. Comerford & Greene 2014; Allen et al. 2015; Hampton et al. 2017).

In this work, we used data from the Mapping Nearby Galaxies at Apache Point Observatory (MaNGA) survey (Bundy et al. 2015). We were motivated to consider these data due to the existence of previous galaxy selections by Rembold et al. (2017), which included a large sample of objects with confirmed AGNs and their control sample containing non-active galaxies. This advantage provides an excellent opportunity to compare the direct AGN estimates with those obtained from oxygen extrapolation gradients, as they cover larger parts of the disc in galaxies, including the nuclear region. Additionally, it is useful to compare metallicity estimates in AGNs hosts sample with a sample of control galaxies, in order to verify if there is any different effect on the metallicity gradient between them. This paper is organized as follows: In Section 2, a brief description of the sample of objects is presented as well as the methods used for estimating the oxygen abundance of the AGNs and the oxygen abundance gradients of the sample. In Section 3, we present the results and discussion. In Section 4, the summary and the conclusions are presented.

2 METHODOLOGY

We selected from the MaNGA data base (Bundy et al. 2015) a sample of spiral galaxies hosting AGNs. The emission-line intensities of the AGN and strong-line calibrations proposed in the literature were used to estimate the oxygen abundances of these objects. In addition, emission-line intensities of star-forming regions located along the disc were used to calculate the oxygen abundance gradient in each galaxy of the sample, and calibrations available in the literature were also considered. In the subsequent sections, a description of the methodology adopted to obtain the observational data and the abundance values are presented.

2.1 Observational data

The sample of galaxies studied here comprise both galaxies hosting AGNs as well as a sample of control galaxies selected as in Rembold et al. (2017). For each AGN, two control non-active galaxies matching the AGN host stellar mass, morphology, distance, and inclination were chosen. After the release of the MaNGA Product Launch 8 (MPL-8; Gunn et al. 2006; Smee et al. 2013; Drory et al. 2015; Law et al. 2015, 2016; Yan et al. 2016; Blanton et al. 2017; Wake et al. 2017; MPL-8, Aguado et al. 2019), the number of observed AGNs with MaNGA has grown to 170 AGNs and 291 control galaxies as described in Riffel et al. (2021). We classified the nuclei (central region with 2.5-arcsec diameter) and the regions along the disc of the galaxies according to their emission-line ratios in the diagnostic diagram [O III]λ5007/Hα versus [N II]λ6584/Hα, proposed by Baldwin, Phillips & Terlevich (1981, hereafter called BPT diagram) and on the WHAN diagram proposed by Cid Fernandes et al. (2010).

First, to classify the regions in the sample as AGN-like and H II-like objects, we used the theoretical and the empirical criteria proposed by Kewley et al. (2001) and Kauffmann et al. (2003), respectively. These criteria establish that regions with

$$\log([\mathrm{O\,III}]\lambda5007/\mathrm{H}\beta) > \frac{0.61}{\log([\mathrm{N\,II}]\lambda6584/\mathrm{H}\alpha) - 0.47} + 1.19 \quad (1)$$

and

$$\log([\mathrm{O\,III}]\lambda5007/\mathrm{H}\beta) < \frac{0.61}{\log([\mathrm{N\,II}]\lambda6584/\mathrm{H}\alpha) - 0.05} + 1.3 \quad (2)$$

are classified as AGN-like objects, otherwise, as H II-like objects. Additionally, we applied the criterion proposed by Cid Fernandes et al. (2010) to separate AGN-like and LINER objects, given by

$$\log([\mathrm{O\,III}]\lambda5007/\mathrm{H}\beta) > 0.47 + \log([\mathrm{N\,II}]\lambda6584/\mathrm{H}\alpha) \times 1.01, \quad (3)$$

where the values satisfying the above criterion correspond to Seyferts, otherwise, they are classified as LINERs. Secondly, for each spaxel of the objects of our sample, the WHAN diagram proposed by Cid Fernandes et al. (2010), which takes into account the equivalent width of Hα versus the [N II]λ6584/Hα line ratio, was considered

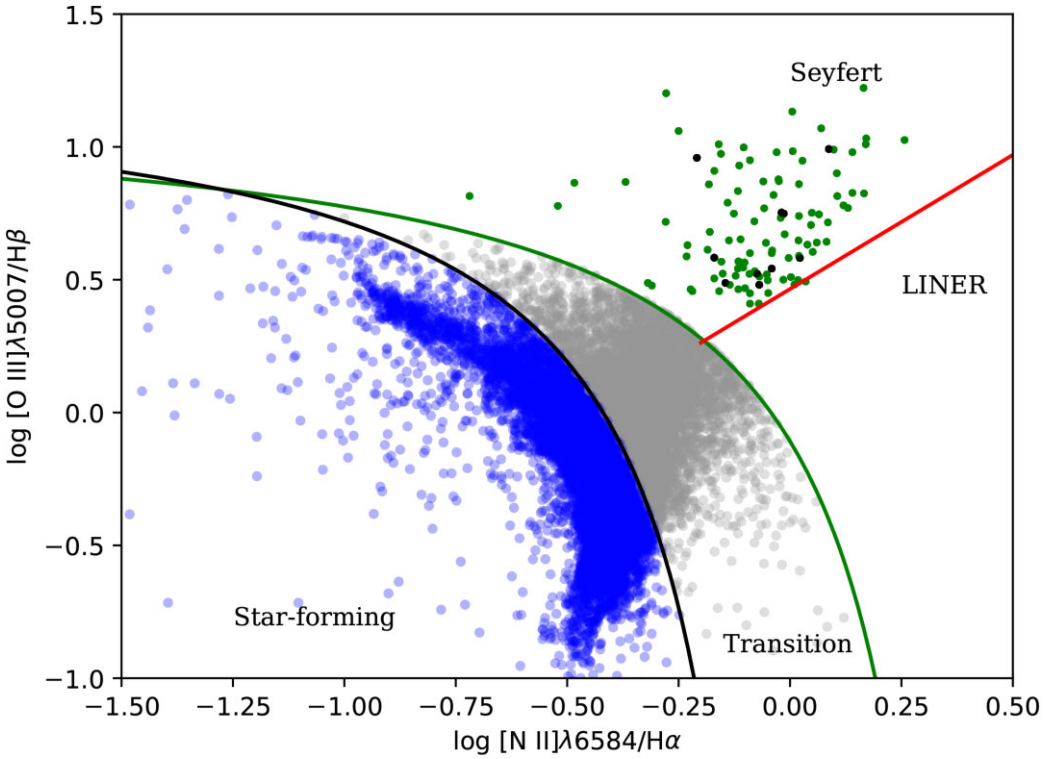

Figure 1. [O III]λ5007/H β versus [N II]λ6584/H α diagnostic diagram for the AGN sample. The green (Seyfert 2) and the black points (Seyfert 1) correspond to the emission-line ratios of the AGNs, obtained by summing the fluxes of all spaxels within an aperture of 2.5 arcsec in diameter in the central region of each galaxy. The blue and grey points are star-forming and transition regions, respectively, whose emission-line ratios were obtained from each spaxel of the data cubes. Black and green lines correspond to the empirical and theoretical criteria to separate AGN- and H II-like objects proposed by Kauffmann et al. (2003) and Kewley et al. (2001), i.e. equations (1) and (2), respectively. The red line represents the criterion proposed by Cid Fernandes et al. (2010) to separate AGN-like and LINERs (equation 3).

to classify AGN-like and H II-like objects. This same procedure has been previously illustrated and applied in do Nascimento et al. (2019).

After applying the aforementioned classification criteria, we selected the Seyfert-type galaxies for our analysis using the final sample that consist of 98 Seyfert 2 and 10 Seyfert 1[1] galaxies as well as their respective control galaxies (145 in the total) for this study. Among the 108 Seyfert galaxies, 71 are also classified as Seyfert using Sloan Digital Sky Survey (SDSS; York et al. 2000), III/Baryonic Oscillation Spectroscopic Survey (BOSS) collaboration data, and flux measurements from Thomas et al. (2013) – the procedure originally used to identify the AGNs in the first paper of our series (Rembold et al. 2017). The remaining 26 are classified as LINERs on the basis of SDSS-III data. The larger number of Seyfert nuclei identified in the MaNGA data than those obtained using the 3.0-arcsec diameter SDSS-III fiber measurements, which is likely due to the better angular resolution of MaNGA. As gas surrounding the Seyfert region frequently shows LINER excitation (e.g. do Nascimento et al. 2019), the larger aperture of the SDSS-III data should be including more of the surrounding LINER region, as well as the possible contribution of emission from gas ionized by extra-nuclear evolved stars, moving the borderline objects from the Seyfert region to the LINER region of the BPT diagram. The radial oxygen gradient in each object covers a region measured in effective radii (R_e) ranging from ∼0.5 to ∼2.5 (see also Mingozzi et al. 2020).

The median point spread function (PSF) of the MaNGA datacubes is estimated to have a full width at half-maximum (FHWM) of about 2.5 arcsec (Law et al. 2015), which can be considered the resolution element in the data. The redshift values of our sample are in the range $0.02 \lesssim z \lesssim 0.08$. Assuming a spatially flat cosmology with $H_0 = 71$ km s^{-1}Mpc^{-1}, $\Omega_m = 0.270$, and $\Omega_{vac} = 0.730$ (Wright 2006), each resolution element represents a region with diameters in the range ∼1-4 kpc at the distance of the MaNGA sample. Thus, since H II regions have typical sizes of tens to a few hundreds parsecs, each resolution element spectrum comprises the flux of a complex of H II regions (Belfiore et al. 2017), and the physical properties derived represent an average value of these regions (e.g. Hagele et al. 2008; Krabbe et al. 2014; Rosa et al. 2014). However, this fact has little influence on the radial oxygen abundance in spiral galaxies because it is expected that H II regions located at similar galactocentric distances present about the same metallicity (e.g. Kennicutt et al. 2003) and similar stellar content (e.g. Dors et al. 2017; Zinchenko et al. 2019).

Following Ilha et al. (2019), the emission-line fluxes from the MaNGA data cube were obtained by fitting a single-Gaussian component using the Gas AND Absorption Line Fitting (GANDALF; Sarzi et al. 2006) routine. The choice of this routine was due to the fact that it fits both the stellar population spectra and the profiles of the emission lines, after the subtraction of the stellar population contribution. A detailed description of the fitting procedure is presented in Ilha et al. (2019).

In Fig. 1, we present the BPT diagram for the central region of the AGN and all other spaxels for the AGN and control sample that

[1]The Seyfert 1 classification was obtained by visual inspection of all nuclear spectra, looking for the presence of broad components in H α and other Balmer lines.

correspond to H II and transition regions. The red line – marking the separation between Seyfert and LINER excitation – was obtained from Kewley et al. (2006); the green line – marking the separation between the transition and AGN regions – was obtained from Kewley et al. (2001); and the black line – marking the separation between the starburst and transition regions – was obtained from Kauffmann et al. (2003). Black circles and green triangles correspond to the emission-line ratios for the AGNs, obtained by summing the fluxes of all spaxels within a central aperture of 2.5-arcsec diameter. The Seyfert 2 galaxies are represented by the black circles and Seyfert 1 by the green triangles. Blue points are star-forming regions and grey points are transition regions. The diameter of the AGN nucleus of the galaxies is based on a fixed angular diameter of 2.5 arcsec and it ranges from ∼1 to ∼6 kpc according to the distance of each object. Thus, for some AGNs, an extended emission is observed.

2.2 Gas-phase metallicity determinations

We estimated the gas-phase metallicity in relation to the solar value ($Z/Z_{\odot}$) for each AGN and the oxygen radial gradients along the disc of each galaxy of the sample.

In the AGN and in the disc, H II region spectra of our sample emission lines sensitive to the electron temperature (e.g. [O III]λ4363, [N II]λ5755) were not detected and, consequently, it was not possible to calculate the elemental abundances by using the T_e-method. Therefore, the O/H abundance or the metallicity was calculated through calibrations based on strong emission lines. Several authors have investigated the O/H discrepancy values obtained when distinct methods are assumed and differences up to 0.6 dex have been found for H II regions (e.g. Kewley & Ellison 2008; Lòpez-Sanchez et al. 2012; Peña-Guerrero, Peimbert & Peimbert 2012). Almost the same discrepancy (i.e. up to 0.8 dex) is also derived for metallicity AGN estimates taking into account different methods, being the highest discrepancy values derived for the low-metallicity regime ($12 + \log(O/H) \lesssim 8.5$; Dors et al. 2020b).

For H II regions, there seems to be a consensus that reliable calibrations are those that produce O/H values similar (or near) to values derived through the T_e-method (see Peimbert, Peimbert & Delgado-Inglada 2017; Pérez-Montero 2017 for a review). For AGNs, it is available in the literature theoretical (Storchi-Bergmann et al. 1998), semi-empirical (Castro et al. 2017; Carvalho et al. 2020; Dors et al. 2021), and empirical (Dors 2021) calibrations between strong optical narrow emission lines and the metallicity or abundances. The recent empirical calibration for AGNs proposed by Dors (2021) requires measurements of the [O II]λ3727[2] emission line, which is not available in our data. Thus, it is not possible to use this calibration in our study. It is beyond the scope of this work to investigate the O/H abundance discrepancy estimations in H II regions and AGNs derived when distinct methods are considered. However, it is worth to stress that the abundance values derived in this work can vary according to the calibrations assumed. In what follows the calibrations used to estimate the radial O/H abundance gradients and the AGN metallicity in our sample are presented.

2.3 H II region calibrations

Since the pioneering work of Pagel et al. (1979), several authors have proposed calibrations between strong emission lines and O/H abundance for H II regions. In particular, the first empirical calibration considering O/H abundances derived through the T_e-method was the one proposed by Storchi-Bergmann, Calzetti & Kinney (1994), where the N2 = log([N II]λ6584/H α) line ratio was considered as metallicity indicator. Afterwards, Pilyugin (2000), Pilyugin (2001) improved this methodology taking into account the [O II]λ3727 and [O III]λ5007 emission lines.

In order to derive the oxygen abundance of H II regions along the galaxy disc of our sample and for the control sample (in the nuclei and in the disc H II regions), we considered the assumption that calibrations based on O/H calculated via the T_e-method (empirical calibrations) more reliable in comparison with theoretical calibrations. In this sense, we assumed the following empirical calibrations proposed by Pérez-Montero & Contini (2009):

$$12 + \log(O/H) = 8.74 - 0.31 \times O3N2, \quad (4)$$

where

$$O3N2 = \log\left(\frac{([O\,III]\,\lambda5007)}{(H\,\beta)} \times \frac{(H\,\alpha)}{([N\,II]\,\lambda6584)}\right). \quad (5)$$

This relation is valid for $12 + \log(O/H) \gtrsim 8.0$. The O3N2 index was introduced by Alloin et al. (1979) as a metallicity indicator. The other calibration considered in this work is based on the N2 parameter:

$$12 + \log(O/H) = 9.07 + 0.79 \times N2. \quad (6)$$

The distribution of O/H values along the disc of the Seyfert 2 galaxy MaNGA ID 1-210646 as well as for its two control galaxies are shown in the second column of Fig. 3. Analogous figures to Fig. 3 are available as supplementary material for the remaining galaxies. The O/H values obtained from the above relations (i.e. equations 4 and 6 for all the spaxels were used to obtain radial abundance gradients along the disc of each galaxy, following the methodology proposed by Riffel et al. 2021). Thus, we have obtained mean azimuthal values and standard deviations for O/H in radial bins of 2.5 arcsec along the galaxy discs. Thereafter, we used the following relation to fit the radial abundance distributions:

$$Y = Y_0 + grad\ Y \times R, \quad (7)$$

where Y is a given oxygen abundance [in units of 12+log(O/H)], R is the galactocentric distance (in units of arcsec), Y_0 is the extrapolated value of the gradient to the Galactic Centre ($R = 0$), and $grad\ Y$ is the slope of the distribution (in units of dex arcsec^{-1}). The third column in Fig. 3 shows these gradients for the Seyfert 2 galaxy with MaNGA ID 1-210646 and its control galaxies.

2.4 AGN calibrations

The O/H abundance in each AGN was derived using its measured emission-line ratios and two calibrations, one proposed by Storchi-Bergmann et al. (1998) and the other recently proposed by Carvalho et al. (2020). In what follows, descriptions of these calibrations are presented.

2.4.1 Storchi-Bergmann et al. (1998) calibration

Storchi-Bergmann et al. (1998), by using a grid of photoionization models built with the CLOUDY code (Ferland et al. 2017), proposed two theoretical calibrations between the emission-line ratios [N II]λ6584/H α, [O III]λ5007/[O II]λ3727, and [O III]λ5007/H α and the metallicity (traced by the O/H abundance). These calibrations are valid for the range of $8.4 \leq 12 + \log(O/H) \leq 9.4$ and the O/H

[2][O II]λ3727 corresponds to the sum of the λ3726 and λ3729 emission lines.

abundances obtained from these calibrations differ by only ∼0.1 dex (Storchi-Bergmann et al. 1998; Dors et al. 2020b).

In this work, we used only one calibration proposed by Storchi-Bergmann et al. (1998, hereafter SB_1) because the [O II]λ3727 is not available in our data set. The SB_1 calibration is defined by

$$\begin{aligned} 12 + (\mathrm{O/H})_{\mathrm{SB_1}} &= 8.34 + (0.212\,x) - (0.012\,x^2) - (0.002\,y) \\ &+ (0.007\,xy) - (0.002\,x^2y) + (6.52 \times 10^{-4}\,y^2) \\ &+ (2.27 \times 10^{-4}\,xy^2) + (8.87 \times 10^{-5}\,x^2y^2), \end{aligned} \quad (8)$$

where $x = [\mathrm{N\,II}]\lambda\lambda6548,6584/\mathrm{H}\,\alpha$ and $y = [\mathrm{O\,III}]\lambda\lambda4959,5007/\mathrm{H}\,\beta$. In order to take into account the dependence of this relation on the gas electron density (N_e), we applied the correction proposed by these authors:

$$\log(\mathrm{O/H})_{\mathrm{SB98f}} = [\log(\mathrm{O/H})_{\mathrm{SB_1}}] - \left[0.1 \times \log \frac{N_e(\mathrm{cm^{-3}})}{300\ (\mathrm{cm^{-3}})}\right]. \quad (9)$$

The electron density (N_e), for each object, was calculated from the [S II]λ6716/λ6731 line ratio, using the IRAF/TEMDEN task and assuming an electron temperature of 10 000 K.

2.4.2 *Carvalho et al. (2020) calibration*

Carvalho et al. (2020), by using a diagram [O III]λ5007/[O II]λ3727 versus [N II]λ6584/H α, compared observational data of 463 Seyfert 2 nuclei ($z \lesssim 0.4$) with photoionization model predictions built with the CLOUDY code (Ferland et al. 2017), which considered a wide range of nebular parameters. From this comparison, they obtained a semi-empirical calibration between the N2 = log([N II]λ6584/H α) line ratio and the metallicity Z given by

$$(Z/Z_\odot) = 4.01^{\mathrm{N2}} - 0.07, \quad (10)$$

valid for $0.3 \lesssim (Z/Z_\odot) \lesssim 2.0$. The metallicity results obtained from the expression above can be converted into oxygen abundance by

$$12 + \log(\mathrm{O/H})_C = 12 + \log\left[(Z/Z_\odot) \times 10^{\log(\mathrm{O/H})_\odot}\right], \quad (11)$$

where $\log(\mathrm{O/H})_\odot = -3.31$ is the solar value (Alende Prieto, Lambert & Asplund 2001). The N2 index has an advantage over other metallicity indicators because it involves emission lines with very close wavelength: Thus, N2 is not strongly affected by dust extinction and uncertainties produced by flux calibration (Marino et al. 2013) as the O3N2. However, due to the fact that N2 and O3N2 indices involve the ions N^+, O^{2+}, and H^+ that have different ionization potentials, i.e. 29.60, 54.93, and 13.6 eV, respectively, they have a higher dependence on the ionization degree of the gas phase than other indices, for instance, N2O2. Recently, Kumari et al. (2019) suggested that O3N2 index can be used as a metallicity tracer of the diffuse ionized gas (DIG) and of low-ionization emission regions [LI(N)ERs] in passive regions of galaxies These authors also pointed out that the O3N2 could also be extended for metallicity estimates in Seyferts. Further calibrations involving the O3N2 could produce additional gas-phase metallicity estimations in Seyferts, supporting the results obtained in this work, hence it is used as the H II region metallicity diagnostic.

Regarding the electron density effect on the strong-line calibrations, in general, NLRs of AGNs present higher N_e values in comparison with the ones in the gas phase of H II regions. For instance, Copetti et al. (2000), adopting the [S II]λ6716/λ6731 as an N_e indicator, derived electron density values for a sample of galactic H II regions in the range of $N_e \approx 20 - 400$ cm^{-3} (see also, Krabbe et al. 2014; Mora et al. 2019; Buzzo et al. 2021; Rosa et al. 2021). On the other hand, electron density estimates in AGNs based on [S II]λ6716/λ6731 and [Ar IV]λ4711/λ4740 line ratios by Congiu et al. (2017) show values ranging from ∼200 to 13 000 cm^{-3} (see also Freitas et al. 2018; Kaddad et al. 2018; Revalski et al. 2018; Mingozzi et al. 2019; Davies et al. 2020). It is worthwhile to state that some emission lines with low critical density N_c (e.g. the [O II]λ3727 and [S II]λ6716 lines have $N_c = 10^{3.7}$ and 1600 cm^{-3}, respectively; Vaona et al. 2012) are used in AGN strong-line methods (SB_1; Castro et al. 2017) and can suffer collisional de-excitation. Therefore, it is more important to consider electron density effects on oxygen abundance obtained through strong-line methods for AGNs rather than for H II regions. In any case, the empirical H II region calibrations proposed by Pérez-Montero & Contini (2009) and the semi-empirical AGN calibration proposed by Carvalho et al. (2020) are obtained by using observational data of large samples of objects, with a wide range of nebular parameters. Therefore, in these calibrations, effects of electron density N_e (as well as reddening correction, gas ionization degree, etc.) on emission-line ratio intensities are considered in intrinsic way. On the other hand, the theoretical SB_1 calibration was based on photoionization models, which the electron density was an input parameter. Therefore, these authors proposed a correction technique to take into account the N_e effect on the resulting O/H abundances. However, since typical N_e values in NLRs are around 500 cm^{-3} (see e.g. fig. 2 of Dors 2021), the use of equation (9) implies a correction in the total oxygen abundance of only ∼0.02 dex. Moreover, even considering the highest N_e value found by Dors (2021) for a large sample of Seyfert nuclei, i.e. $N_e = 2250$ cm^{-3}, the O/H correction according to equation (9) is ∼0.1 dex, i.e. lower than the uncertainty of ∼0.2 dex in abundance estimates derived from strong-line methods (e.g. SB_1; Denicoló, Terlevich & Terlevich 2002; Marino et al. 2013). Thus, electron density has a marginal effect on the abundances derived from our sample.

We define the discrepancy D (in dex) as being the difference between the O/H abundance of the AGN (derived from SB_1 or Carvalho et al. 2020 calibrations) and the intersect oxygen abundances derived

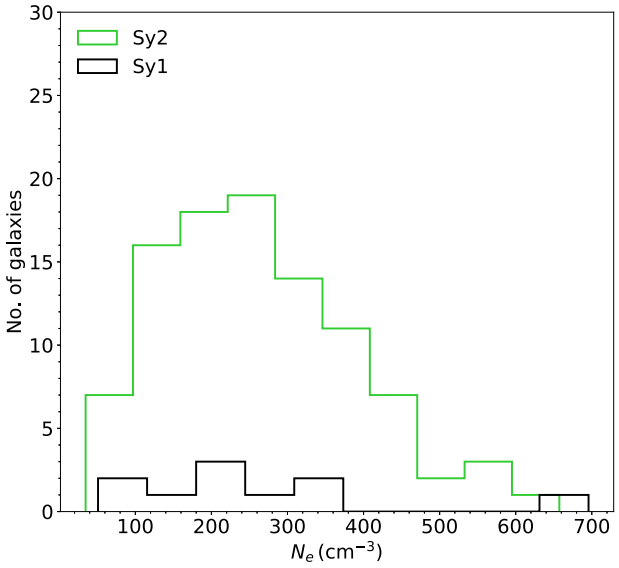

Figure 2. Electronic density distributions obtained within the 2.5-arcsec central region for the 107 AGNs of our sample. The distribution for Seyfert 1 and Seyfert 2 are represented in black and green colours, respectively.

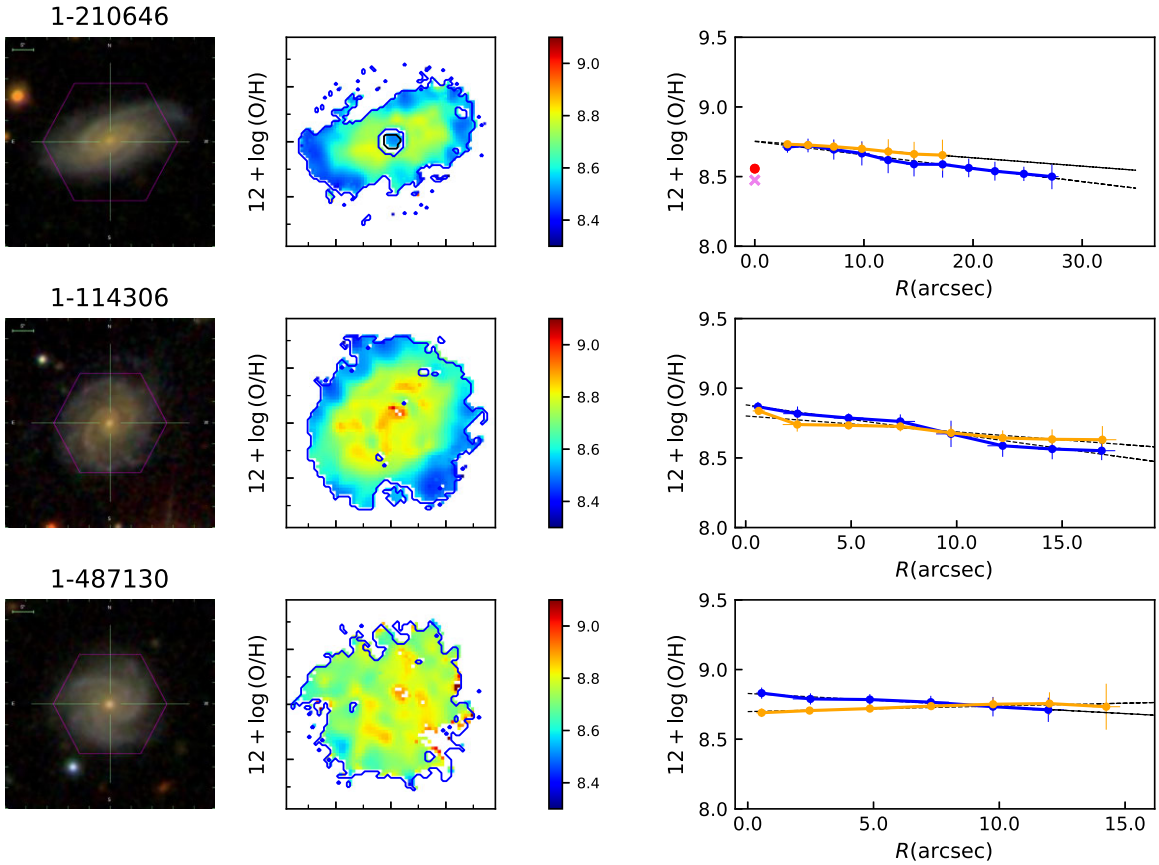

Figure 3. Surface distribution of the gas abundances for the Seyfert 2 galaxy MANGA ID 1-210646 (top row) and its two controls (bottom rows). The tick marks in the maps are separated by 5 arcsec. The left-hand column shows the SDSS-IV images in the bands *gri* with the MaNGA footprint overplotted in pink for the AGN (top panel) and its controls (bottom panel); central column: the metallicity distribution derived assuming the Carvalho et al. (2020) calibration for the AGN region (top row) and the Pérez-Montero & Contini (2009) calibrations for the H II regions in the disc of both the AGN and control galaxies (bottom rows); right-hand column: mean azymuthal profile and standard deviations of the oxygen abundance (in units of 12+log(O/H)). The profile in blue was obtained from equation (4) and the one in orange was obtained from equation (6), and are plotted versus the galactocentric distance R (in units of arcsec). In the top panel showing the AGN gradient, the central values obtained from the calibration proposed by Carvalho et al. (2020) and Storchi-Bergmann et al. (1998) are shown in red point and pink cross sign point, respectively.

from the radial abundance gradients:

$$D = [12 + \log(\mathrm{O/H})_{\mathrm{AGN}}] - [12 + \log(\mathrm{O/H})_0], \quad (12)$$

where $12 + \log(\mathrm{O/H})_0 \equiv Y_0$.

3 RESULTS AND DISCUSSION

In Fig. 2, we present the electron density distribution obtained within the 2.5-arcsec central region, for the 108 Seyfert galaxies. The black and green distributions represent the results for Seyfert 1 and Seyfert 2 nuclei, respectively. The maximum and minimum values, taking into account the total sample of Seyfert 1 and Seyfert 2, are 696 and 35 cm^{-3} respectively, with the mean value of $N_e \approx$ 260 cm^{-3} and a median value of $N_e \approx 240$ cm^{-3}. The range of N_e values derived from our sample is somewhat lower than the N_e values obtained by Dors et al. (2020a), who derived the range $100 \lesssim N_e\,(\mathrm{cm}^{-3}) \lesssim 10\,000$ and an average value of ∼650 cm^{-3}, for a sample of 463 Seyfert 2 nuclei whose data were taken from the SDSS DR7 (York et al. 2000). However, only 15 per cent of the objects considered by Dors et al. (2020a) present higher N_e values than the maximum value derived from our sample. Vaona et al. (2012) selected about 2700 spectra of Seyfert nuclei from SDSS DR7 (York et al. 2000) and, among other nebular properties, estimated N_e mainly based on the [S II]λ6716/6731 line ratio. These authors derived a range of values similar to the estimations by Dors et al. (2020a) and an average value of $N_e \sim 250$ cm^{-3}, whereby most of the objects (∼ 2300 galaxies) show values lower than 500 cm^{-3}, while higher electron density values greater than 1000 cm^{-3} were derived from only 97 (∼ 3 per cent) objects (see also Zhang et al. 2013). Thus, the discrepancy in N_e values above is probably due to the distinct and larger sample of objects considered by Dors et al. (2020a) and Vaona et al. (2012). It is worth mentioning that the N_e values obtained from our sample are well below the critical density value (N_c) of the emission lines considered in this work. In fact, the emission line with the lowest N_c is [S II]λ6716 ($N_c \sim 1600$ cm^{-3}, Vaona et al. 2012), indicating that the collisional de-excitation is negligible in this case, which also does not affect the emissivity of the lines and, consequently, the chemical abundance estimations (for a detailed discussion on electron density effects on AGN abundance determinations, see Dors et al. 2020a).

We derived spatially resolved maps and radial chemical abundance profiles for the AGN together with controls and showing the corresponding maps for the galaxy with MaNGA ID 1-210646 (AGN) and its controls in Fig. 3. The maps for the remaining objects are shown in Figs A1–A72. The radial profiles were corrected for projection, using information about the major and minor axis (from

SDSS galaxy image, obtained from the MaNGA's drpall table) to determine the inclination of the galaxies. The inclination angle of the AGN sample and their controls range from 1° to 70° (the control galaxies were chosen to match each of the selected AGN hosts). We were able to obtain the O/H radial gradients for 61 galaxies containing AGNs (from a total sample of 108 galaxies hosting AGNs) and for 112 control galaxies (from a sample of 145 control galaxies). The chemical abundance profiles shown in blue and orange in Figs 3 and A1–A72 were derived by using the calibrations (equations 4 and 6 from Pérez-Montero & Contini 2009). The dashed lines represent the fits of the points by equation (7). The blue and orange points represent the mean values, with standard deviations, considering all spaxels (both from control and AGN galaxies) divided in bins of 2.5-arcsec width. The slopes of the gradients in each galaxy and extrapolated abundances [$Y_0 \equiv 12 + \log(\mathrm{O/H})_0$] to the centre (galactocentric distance $R = 0$) are listed in Table 1.

Fig. 3 and A1–A72 show, in the left-hand panels, the SDSS image in the bands *gri* of each galaxy with the MaNGA footprint overplotted in pink, and in the central panels, maps of the oxygen abundance distribution (in units of 12+log(O/H)) along the galactic discs.

The white regions in these maps represent the spaxels classified as transition objects or LI(N)ER-like objects (see also Kaplan et al. 2016) for which the calibrations used in this work can not be applied. Although recent studies (Kumari et al. 2019; Wu 2020, 2021) have investigated metallicity derivation in these object class, we did not obtain any estimate for them. For about 43 per cent of the AGN sample it was not possible to obtain the radial abundance gradient due to the fact that the spaxels in the disc are not classified as SF-like objects in the diagnostic diagram (see Fig. 1), i.e. they are classified as transition or AGN-like objects. These objects may include disc regions with a composite ionization source, such as shocks mixed with ionization from a young stellar cluster (e.g. see Allen et al. 2008; Rosa et al. 2014). Transition objects are indeed expected to have a stellar cluster–AGN mixing as their ionizing source (e.g. Kewley et al. 2006; Wu et al. 2007; Davies et al. 2014). Although recent studies have proposed methods to estimate the metallicity in this class of objects (i.e. composite objects; see e.g. Wu 2020, 2021), we did not estimate the abundances for them because the main goal of this work is the comparison between AGN and H II region metallicities.

Regarding the metallicity gradients presented in the right-hand panels of Fig 3 and A1–A72 (for the AGN host disc and its control galaxies), we can state that: in the AGN host disc, the metallicity gradient is comparable to that found in the control galaxies; although we have used two different calibrations for the H II regions – the blue profile derived from the O3N2 index (equation 5) and the orange profile from the N2 index (equation 6) – show similar gradients that are mostly negative. Our main findings are as follows:

(i) ∼66 per cent of the galaxies containing AGNs have negative radial gradients when these are derived via O3N2 and N2 indices (i.e. the O/H abundance decreases as the galactocentric distance increases);

(ii) ∼25 per cent of AGN hosts have positive gradients, indicating an increase in metallicity as we move away from the central region; and

(iii) ∼9 per cent of the AGN host sample present flat gradients.

These results are confirmed by the histograms shown in Fig. 4, comparing the central extrapolated abundances and the gradient slopes of the AGN hosts (blue line)

with those from their control galaxies (light green dashed lines).

If galaxies evolve as a closed system and are formed according to the inside-out scenario (e.g. Mollá & Díaz 2005), negative abundance gradients are expected. In fact, this feature is commonly found in most discs of spiral galaxies (e.g. Shaver et al. 1983; van Zee et al. 1998; Kennicutt et al. 2003; Pilyugin, Vílchez & Contini 2004; Dors & Copetti 2005; Sánchez et al. 2014; Belfiore et al. 2017; Mingozzi et al. 2020; Skillman et al. 2020). However, some relevant processes could affect the galaxy evolution resulting in radial gradients that differ from the expected negative abundance gradients. For instance, some galaxies are formed and evolve in a complex environment (galaxies can have a nurture evolution; see Paulino-Afonso et al. 2019 and references therein), with gas circulating inside, outside, and around them, making galaxies evolve in short time-scales (Somerville & Davé 2015). This cycle includes modified star formation, accretion, mergers, and the way each action impacts the galaxy is unique. If metal-poor gas accretion is deposited directly into the centres of galaxies, it should act to dilute the central metallicity, flatten, or push down negative gradients (Simons et al. 2020), producing a break in the gradients at small galactocentric distances.

The histograms in Fig. 5 show the oxygen abundance distributions calculated within the inner 2.5 arcsec of each galaxy, i.e for the AGNs and their control galaxies (which have star-forming nuclei), whose O/H values were derived by using the calibrations described in Section 2. In the left- and right-hand panels of Fig. 5, the AGN abundances calculated by equations (9) and (10) are represented in red and pink colours, respectively. Distributions for the control sample are represented by the hatched area (in light green) and the abundances are estimated using equation (5). In both panels of Fig. 5, it can be seen that the results indicate that control galaxies present O/H abundance values higher than those derived for AGNs.

In Fig. 6, the $12 + \log(\mathrm{O/H})$ values obtained from the AGN calibrations (see Section 2.4) are plotted against those inferred from the gradient extrapolations. The Y_0 values (see equation 7) of the metallicity gradients were determined from the H II region calibrations based on O3N2 (left-hand panels) and N2 (right-hand panels) indices proposed by Pérez-Montero & Contini (2009). In general, it is possible to verify that, even considering the errors in the estimates, i.e. of the order of ±0.1 dex (e.g. DTT02; Marino et al. 2013), the direct estimations for AGNs (derived through SB_1 and Carvalho et al. 2020 calibrations) are lower than the estimates obtained from the gradient extrapolations for the high-metallicity regime ($12 + \log(\mathrm{O/H}) \gtrsim 8.6$). Our findings reveal that:

(i) ∼80 per cent of the metallicity values of AGNs, derived from the SB_1 and Carvalho et al. (2020) calibrations are lower than those obtained via extrapolation methods (using both the N2 and O3N2 relations for the H II regions to derive the disc gradients);

(ii) ∼15 per cent of the metallicity values obtained for the AGNs are similar (within the uncertainties) to those obtained via the extrapolation estimates; and

(iii) for ∼5 per cent of the sample, we found the AGN metallicities derived from the calibrations above higher than the values derived from the extrapolations.

In Fig. 3, both the O/H radial gradients and the estimates for the AGN (based on SB_1 and Carvalho et al. 2020 calibrations) for the Seyfert 2 galaxy with MANGA ID 1-210646 are shown. It can be seen that a break in the radial gradient at small galactocentric distance is observed when considering the values based on the AGN calibrations, while the difference between the two values (or discrepancy) D is of the order of 0.5 dex (see also Fig. 7). In summary, there is a clear tendency of the AGN oxygen abundance (or metallicity) to be lower than the extrapolated O/H value for the high-metallicity regime.

Table 1. Parameters for the 107 Seyfert galaxies of our sample of AGNs in MaNGA-MPL8-.

	N2		O3N2		12+log(O/H)	
ID	Slope	$(O/H)_0$	Slope	$(O/H)_0$	$O/H)_C$	$(O/H)_{SB98f}$
(1)	(2)	(3)	(4)	(5)	(6)	(7)
1-44303	− 0.004 ± 0.001	8.80 ± 0.018	− 0.007 ± 0.002	8.78 ± 0.017	8.65	8.58
1-460812	− 0.004 ± 0.005	8.79 ± 0.087	− 0.006 ± 0.006	8.67 ± 0.121	8.63	8.60
1-24148	–	–	–	–	8.79	8.80
1-163966	− 0.002 ± 0.001	8.80 ± 0.008	− 0.006 ± 0.001	8.81 ± 0.012	8.71	8.71
1-149561	–	–	–	–	8.61	8.52
1-295542	–	–	–	–	8.55	8.45
1-24660	− 0.003 ± 0.002	8.81 ± 0.033	− 0.007 ± 0.001	8.80 ± 0.018	8.67	8.58
1-258373	0.002 ± 0.001	8.74 ± 0.011	0.001 ± 0.002	8.78 ± 0.023	8.61	8.54
1-296733	–	–	–	–	8.65	8.66
1-60653	0.0002 ± 0.001	8.75 ± 0.014	0.0005 ± 0.001	8.73 ± 0.018	8.56	8.52
1-109056	− 0.006 ± 0.003	8.77 ± 0.036	− 0.005 ± 0.001	8.66 ± 0.014	8.62	8.62
1-210646	− 0.006 ± 0.0004	8.75 ± 0.004	− 0.010 ± 0.001	8.75 ± 0.011	8.56	8.47
1-248420	− 0.005 ± 0.001	8.82 ± 0.009	− 0.012 ± 0.003	8.85 ± 0.025	8.67	8.59
1-277552	− 0.007 ± 0.001	8.75 ± 0.012	− 0.005 ± 0.001	8.68 ± 0.016	8.58	8.44
1-96075	− 0.003 ± 0.001	8.77 ± 0.006	− 0.007 ± 0.004	8.79 ± 0.034	8.67	8.56
1-558912	–	–	–	–	8.70	8.62
1-269632	–	–	–	–	8.63	8.52
1-258599	–	–	–	–	8.51	8.50
1-121532	–	–	–	–	8.60	8.59
1-209980	0.010 ± 0.005	8.46 ± 0.071	0.003 ± 0.002	8.48 ± 0.029	8.65	8.57
1-44379	0.002 ± 0.002	8.72 ± 0.025	− 0.002 ± 0.001	8.70 ± 0.011	8.73	8.69
1-149211	–	–	–	–	8.41	8.49
1-279147	–	–	–	–	8.59	8.51
1-94784	− 0.002 ± 0.001	8.77 ± 0.010	0.005 ± 0.001	8.72 ± 0.011	8.76	8.71
1-339094	–	–	–	–	8.58	8.57
1-137883	–	–	–	–	8.58	8.58
1-48116	− 0.0003 ± 0.001	8.81 ± 0.008	0.003 ± 0.001	8.76 ± 0.005	8.61	8.54
1-135641	− 0.002 ± 0.001	8.82 ± 0.017	− 0.001 ± 0.001	8.82 ± 0.013	8.66	8.78
1-248389	–	–	–	–	8.82	8.89
1-321739	− 0.0004 ± 0.0003	8.71 ± 0.013	− 0.0004 ± 0.0004	8.65 ± 0.013	8.59	8.54
1-234618	− 0.0004 ± 0.0001	8.74 ± 0.006	− 0.0004 ± 0.0001	8.67 ± 0.008	8.57	8.59
1-351790	–	–	–	–	8.47	8.67
1-23979	–	–	–	–	8.51	8.49
1-542318	–	–	–	–	8.69	8.62
1-279676	− 0.004 ± 0.003	8.80 ± 0.031	− 0.008 ± 0.005	8.77 ± 0.054	8.64	8.62
1-519742	− 0.017 ± 0.007	8.76 ± 0.039	0.010 ± 0.012	8.56 ± 0.063	8.59	8.63
1-94604	− 0.022 ± 0.008	8.81 ± 0.063	− 0.017 ± 0.003	8.67 ± 0.020	8.67	8.61
1-37036	–	–	–	–	8.71	8.64
1-167688	–	–	–	–	8.56	8.62
1-279666	–	–	–	–	8.68	8.63
1-148068	0.003 ± 0.001	8.73 ± 0.017	− 0.006 ± 0.001	8.83 ± 0.015	8.71	8.60
1-603941	− 0.008 ± 0.001	8.77 ± 0.007	− 0.012 ± 0.001	8.79 ± 0.017	8.61	8.54
1-153627	− 0.004 ± 0.0005	8.80 ± 0.006	− 0.006 ± 0.001	8.75 ± 0.019	8.55	8.58
1-270129	0.003 ± 0.001	8.74 ± 0.006	0.001 ± 0.002	8.77 ± 0.020	8.67	8.56
1-298938	− 0.009 ± 0.001	8.80 ± 0.017	− 0.008 ± 0.002	8.70 ± 0.030	8.61	8.54
1-420924	− 0.003 ± 0.001	8.79 ± 0.014	− 0.002 ± 0.001	8.78 ± 0.016	8.63	8.55
1-626658	− 0.005 ± 0.002	8.79 ± 0.015	− 006 ± 0.002	8.79 ± 0.024	8.67	8.60
1-603039	− 0.001 ± 0.001	8.81 ± 0.012	0.002 ± 0.0005	8.74 ± 0.005	8.60	8.51
1-43868	0.017 ± 0.003	8.64 ± 0.062	− 002 ± 0.001	8.82 ± 0.021	8.70	8.74
1-71987	–	–	–	–	8.62	8.57
1-121973	–	–	–	–	8.75	8.68
1-122304	–	–	–	–	8.66	8.56
1-174631	–	–	–	–	8.49	8.58
1-617323	− 0.001 ± 0.002	8.82 ± 0.020	0.003 ± 0.003	8.77 ± 0.032	8.64	8.62
1-176644	− 0.008 ± 0.004	8.77 ± 0.053	− 0.013 ± 0.003	8.79 ± 0.044	8.74	8.66
1-177972	–	–	–	–	8.55	8.55
1-179679	0.016 ± 0.004	8.68 ± 0.029	− 0.005 ± 0.002	8.81 ± 0.014	8.75	8.76
1-196597	− 0.0005 ± 0.002	8.79 ± 0.040	− 0.001 ± 0.001	8.72 ± 0.017	8.66	8.61
1-210020	− 0.007 ± 0.003	8.86 ± 0.075	− 0.005 ± 0.001	8.70 ± 0.032	8.59	8.56
1-201392	–	–	–	–	8.63	8.54
1-209707	–	–	–	–	8.51	8.51

Table 1 – *continued*

ID	N2		O3N2		12+log(O/H)	
	Slope	$(O/H)_0$	Slope	$(O/H)_0$	$O/H)_C$	$(O/H)_{SB98f}$
1-209772	–	–	–	–	8.67	8.60
1-633942	−0.006 ± 0.001	8.82 ± 0.010	−0.005 ± 0.001	8.77 ± 0.015	8.74	8.70
1-277257	0.0005 ± 0.001	8.72 ± 0.018	0.004 ± 0.002	8.59 ± 0.027	8.60	8.63
1-298778	0.002 ± 0.001	8.78 ± 0.004	0.013 ± 0.005	8.70 ± 0.032	8.77	8.78
1-299013	−0.012 ± 0.001	8.85 ± 0.012	−0.018 ± 0.003	8.84 ± 0.026	8.67	8.72
1-323794	0.001 ± 0.002	8.66 ± 0.037	0.001 ± 0.001	8.59 ± 0.030	8.54	8.53
1-384124	–	–	–	–	8.63	8.60
1-405760	–	–	–	–	8.61	8.58
1-625513	−0.009 ± 0.001	8.84 ± 0.016	0.008 ± 0.001	8.76 ± 0.023	8.57	8.52
1-519412	–	–	–	–	8.45	8.46
1-547402	−0.001 ± 0.003	8.88 ± 0.72	−003 ± 0.003	8.59 ± 0.069	8.47	8.52
1-175889	0.002 ± 0.001	8.73 ± 0.010	0.001 ± 0.002	8.75 ± 0.030	8.59	8.54
1-605353	−0.008 ± 0.002	8.84 ± 0.020	−0.011 ± 0.003	8.82 ± 0.029	8.77	8.86
1-232143	−0.011 ± 0.001	8.73 ± 0.013	−0.015 ± 0.001	8.73 ± 0.010	8.45	8.46
1-251458	0.001 ± 0.001	8.77 ± 0.008	−0.001 ± 0.004	8.82 ± 0.023	8.69	8.64
1-298298	−0.004 ± 0.001	8.75 ± 0.011	−0.004 ± 0.001	8.72 ± 0.013	8.57	8.61
1-380097	−0.002 ± 0.0004	8.78 ± 0.003	0.001 ± 0.003	8.74 ± 0.023	8.60	8.51
1-31788	0.002 ± 0.001	8.79 ± 0.008	0.0002 ± 0.002	8.75 ± 0.022	8.56	8.49
1-46056	–	–	–	–	8.54	8.54
1-114252	–	–	–	–	8.64	8.57
1-150947	0.008 ± 0.003	8.67 ± 0.034	0.010 ± 0.002	8.57 ± 0.018	8.55	8.50
1-604912	0.002 ± 0.004	8.82 ± 0.056	−0.003 ± 0.003	8.78 ± 0.037	8.58	8.53
1-145679	0.003 ± 0.001	8.74 ± 0.013	0.003 ± 0.003	8.76 ± 0.036	8.78	8.69
1-163789	−0.048 ± 0.002	9.09 ± 0.017	−0.043 ± 0.008	9.02 ± 0.071	8.65	8.59
1-635348	–	–	–	–	8.76	9.00
1-153901	–	–	–	–	8.62	8.53
1-201969	−0.014 ± 0.007	8.88 ± 0.029	−0.006 ± 0.002	8.95 ± 0.084	8.73	8.66
1-196637	–	–	–	–	8.64	8.59
1-229862	−0.001 ± 0.002	8.80 ± 0.015	−0.012 ± 0.011	8.83 ± 0.087	8.66	8.65
1-229731	0.003 ± 0.0003	8.74 ± 0.003	0.0004 ± 0.001	8.79 ± 0.009	8.69	8.62
1-264729	−0.001 ± 0.0004	8.70 ± 0.023	−0.001 ± 0.0002	8.63 ± 0.009	8.54	8.53
1-268479	−0.012 ± 0.003	8.87 ± 0.030	−0.015 ± 0.002	8.82 ± 0.021	8.68	8.56
1-295041	−0.002 ± 0.001	8.80 ± 0.009	−0.020 ± 0.003	8.84 ± 0.025	8.58	8.54
1-281125	–	–	–	–	8.16	8.42
1-298498	–	–	–	–	8.31	8.41
1-297172	–	–	–	–	8.61	8.55
1-317962	–	–	–	–	8.58	8.47
1-318148	–	–	–	–	8.33	8.45
1-379811	–	–	–	–	8.51	8.47
1-605069	–	–	–	–	8.62	8.56
1-376346	–	–	–	–	8.63	8.55
1-382697	–	–	–	–	8.55	8.51
1-382452	–	–	–	–	8.59	8.56
1-403982	−0.004 ± 0.006	8.81 ± 0.050	−0.001 ± 0.001	8.70 ± 0.008	8.68	8.68
1-605215	−0.005 ± 0.001	8.82 ± 0.007	−0.012 ± 0.001	8.80 ± 0.011	8.63	8.57
1-457424	–	–	–	–	8.72	8.79
1-537120	–	–	–	–	8.73	8.69

Columns. (1) Galaxy identification in the MaNGA survey. (2)–(3) slope (*grad Y*, in units of dex arcsec^{-1}) of the oxygen radial gradient and the extrapolated value of the gradient to the Galactic Centre ($R = 0$) considering the fit of the equation (7) to the abundance estimates along the entire disc of each object and the (O/H)-N2 calibration (equation 6). (4)–(5) Same than for the columns (2)–(3) but for estimations from (O/H)-O3N2 calibration (equation 6). (6)–(7) Estimates of 12 + log(O/H) for the nuclear region of each galaxy obtained through the calibrations proposed by Carvalho et al. (2020) and SB_1, respectively.

The above result is in agreement with some results found in previous studies. For instance, Dors et al. (2015), who used long-slit spectroscopic data obtained by Ho, Filippenko & Sargent (1997), found that the metallicity in the NLR (derived from SB_1 calibration) and in star-forming nuclei, whose metallicity was estimated by using the *C*-method (Pilyugin, Grebel & Mattsson 2012; Pilyugin et al. 2013), are close to or slightly lower than those obtained by the extrapolation method in the regime of high metallicity, i.e. 12+log(O/H)$\gtrsim$ 8.6. These authors pointed out that metal-poor gas accretion is less evident for galaxies with low metallicity, where the metallicity of the accretion material is similar (or not so different) to that of the gas phase in the central regions, therefore, not producing significantly metallicity change. The opposite, probably, occurs for AGNs with high metallicity, where the infalling poor metallicity gas and the one in the galaxy differ considerably. This scenario explains the result shown in Fig. 6. Sánchez et al. (2014) found,

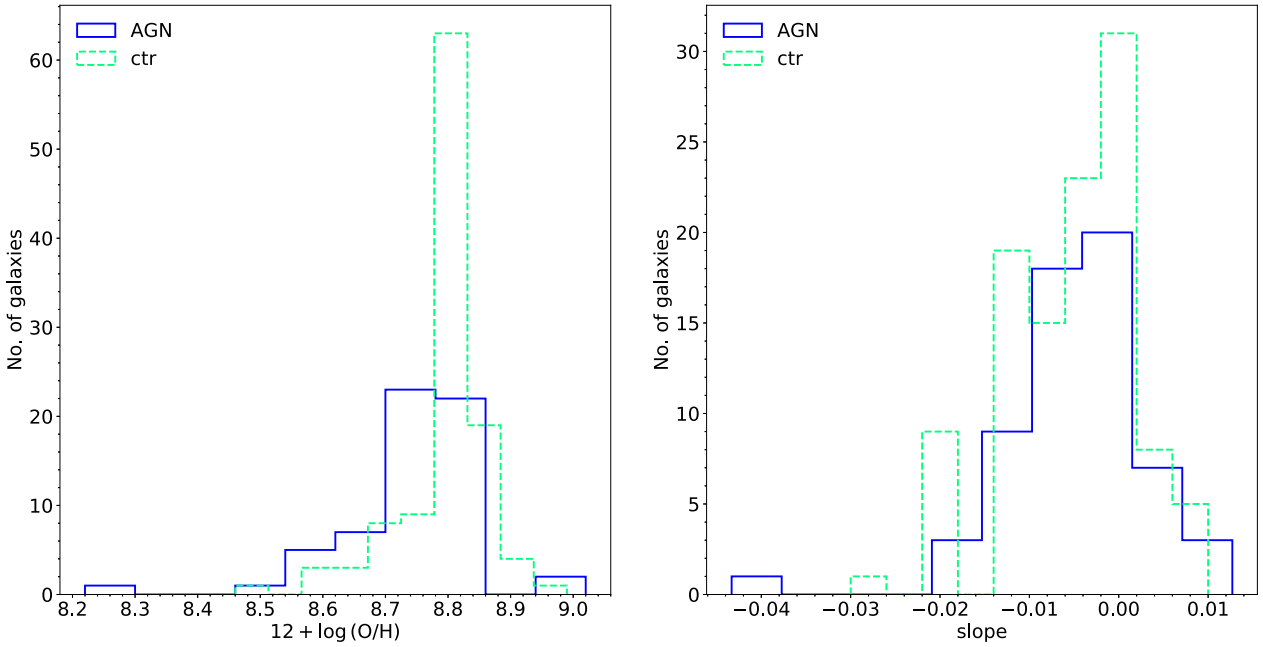

Figure 4. Left-hand panel: distribution of nuclear chemical abundance obtained using the extrapolation method for AGNs and their control galaxies. Both were obtained from the use of the N2 calibration in the H II regions. Right-hand panel: histogram of the slopes of the abundance gradients for the AGNs compared to those from their control galaxies. AGN are shown in blue and the controls in light green dashed lines.

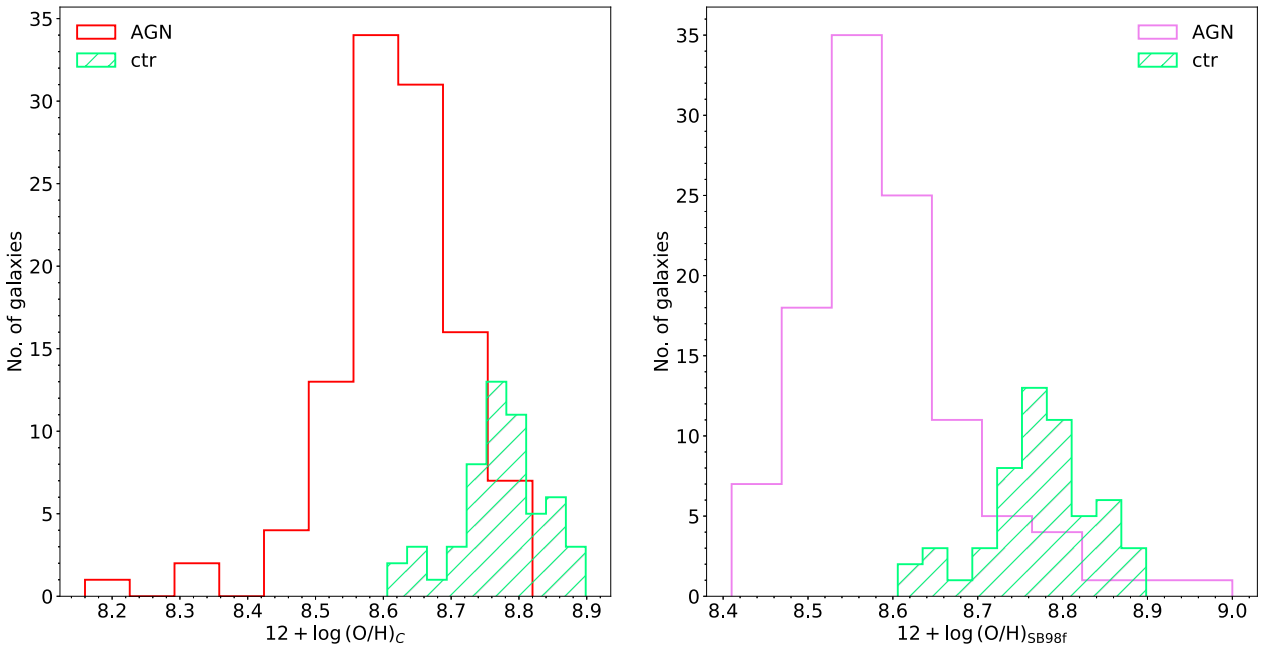

Figure 5. Histograms showing the central oxygen abundances distribution for the AGNs compared to that of the control galaxies. In the left-hand panel, the AGN abundances were obtained using the Carvalho et al. (2020) calibration (red open histogram) and in the right-hand panel using the SB_1 calibration (pink open histogram). The control galaxies are represented by the hatched histogram in light green.

for ∼10 per cent of the objects of the their sample, observational evidence of lower central oxygen abundances than those inferred from the O/H gradient extrapolation to the central parts of spiral galaxies and suggested that a possible explanation is the addition of metal-poor gas to the centre of the galaxies.

To verify if the result shown in Fig. 6 is dependent on the calibration assumed to derive the O/H gradients in our sample, other empirical calibrations were also considered. In particular, we considered the empirical calibrations proposed by DTT02:

$$12 + \log(\mathrm{O/H}) = 9.12 + 0.73 \times \mathrm{N2}, \quad (13)$$

and by PP04:

$$12 + \log(\mathrm{O/H}) = 8.90 + 0.57 \times \mathrm{N2}, \quad (14)$$

and calculated the radial gradients for all objects in our sample.

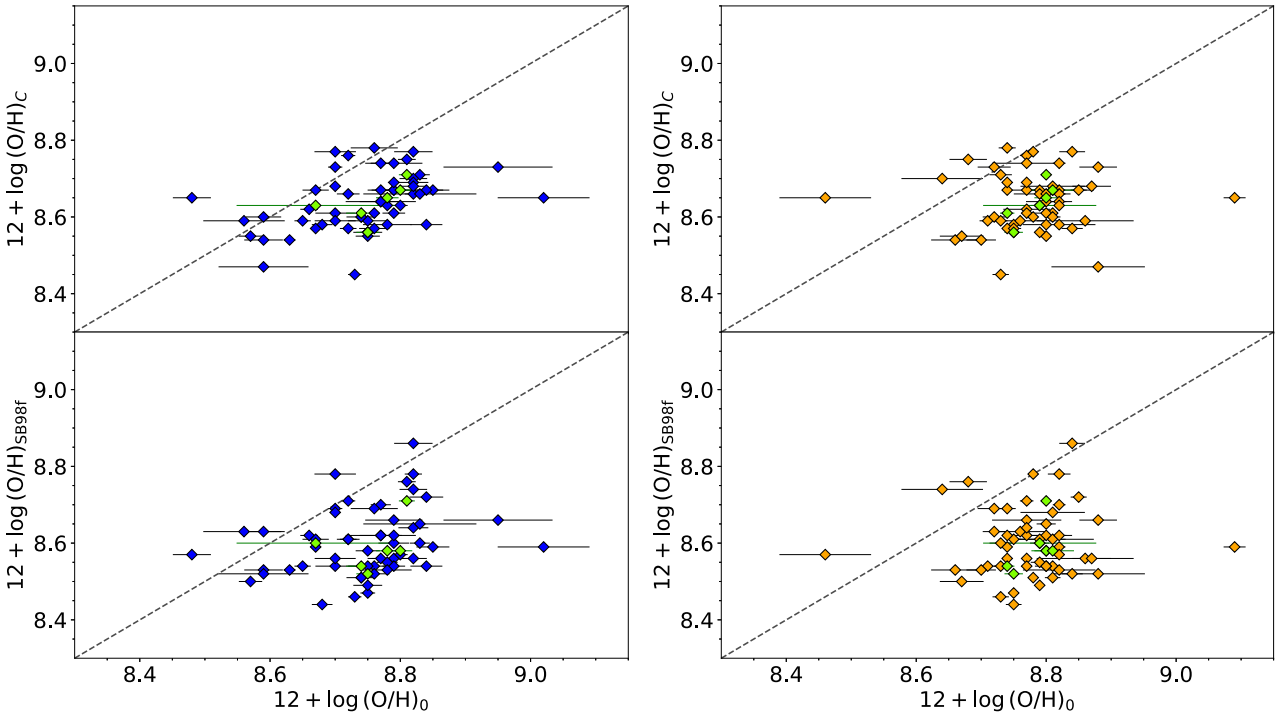

Figure 6. Left-hand panels: 12 + log(O/H) calculated from Carvalho et al. (2020) (top panel) and SB_1 (bottom panel) versus 12 + log(O/H)$_0$ calculated from the O3N2 calibration for the H II regions of PMC09. Right-hand panels: 12 + log(O/H) calculated from Carvalho et al. (2020) (top panel) and SB_1 (bottom panel) versus 12 + log(O/H)$_0$ calculated from the N2 calibration for the H II regions of PMC09. The solid line represents the equality between the estimates.

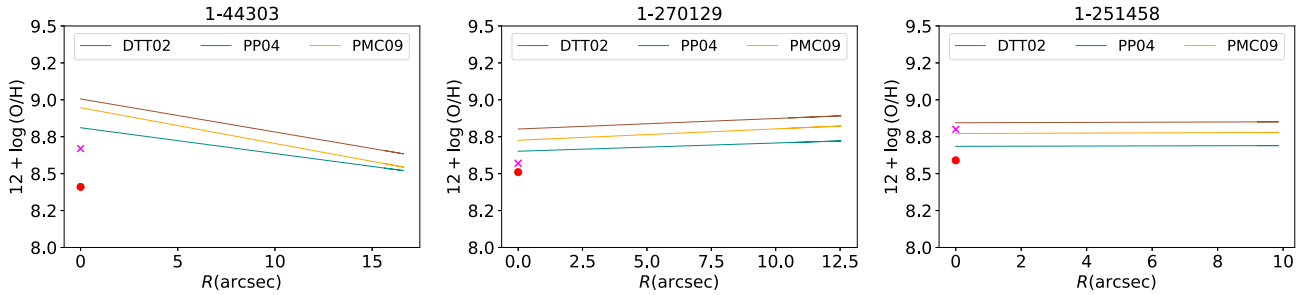

Figure 7. Radial profiles of 12 + log(O/H) obtained by using three different metallicity calibrations for star-forming regions. The lines represent linear regression to the points (not shown): The brown, dark cyan, and orange lines represent linear regressions to the O/H abundance estimates for disc H II regions of each object obtained assuming the calibration by Denicoló et al. (2002, hereafter DTT02) (equation 13), Pettini & Pagel (2004, hereafter PP04) (equation 14), and Pérez-Montero & Contini (2009, hereafter PMC09) (equation 6), respectively. The red point and pink cross sign points represent the abundances for AGN calculated via Carvalho et al. (2020) (equation 10) and SB_1 (equation 8) calibrations, respectively. The error in O/H abundances derived from strong emission line line calibrations is of the order of ±0.1 dex (DTT02).

In Fig. 7, we show the abundance gradients as well as the nuclear abundance values for three AGN hosts, with MANGA ID's 1-44303, 1-270129, and 1-251458, which are representative of the abundance profiles observed in our sample. The resulting O/H gradients based on the three calibrations above are represented by lines with different colours. These gradients were extrapolated to the zero galactocentric distance ($R = 0$). In Fig. 7, the 12+log(O/H) values obtained for the AGNs using the Carvalho et al. (2020) and SB_1 calibrations are also indicated as a red dot and purple cross, respectively. It can be seen that, independently from the calibration considered to derive the gradients in the AGN, with the exception of the object 1-251458, for which the SB_1 calibration produces a high O/H value, we confirm that the extrapolated values are usually higher than those derived from the AGN calibrations. Moreover, the error associated with O/H estimates from calibrations based on strong emission lines is of the order of ±0.1 dex (e.g. DTT02; Marino et al. 2013), lower than the average discrepancy $\langle D \rangle$ (see below) derived for our sample. The rest of the objects (not shown) were subjected to the same process as those in Fig. 7 and yielded similar results.

As discussed previously, there are several physical processes that can produce a decrease (or different O/H abundances) in the O/H abundance (or Z) in the central parts of galaxies in comparison with that obtained from the gradient extrapolation. The simplest scenario appears to be the accretion of metal-poor gas into the nuclear region, e.g. via the capture of a gas-rich dwarf galaxy, which is a process that can lead to the triggering of nuclear activity in galaxies, as discussed in Storchi-Bergmann & Schnorr-Müller (2019). A molecular (e.g. Riffel et al. 2008; Riffel, Storchi-Bergmann & Winge 2013, Moiré et al. 2018) and/or neutral gas (e.g. Allison et al. 2015) reservoir can thus form in the surroundings of the SMBH, feeding it.

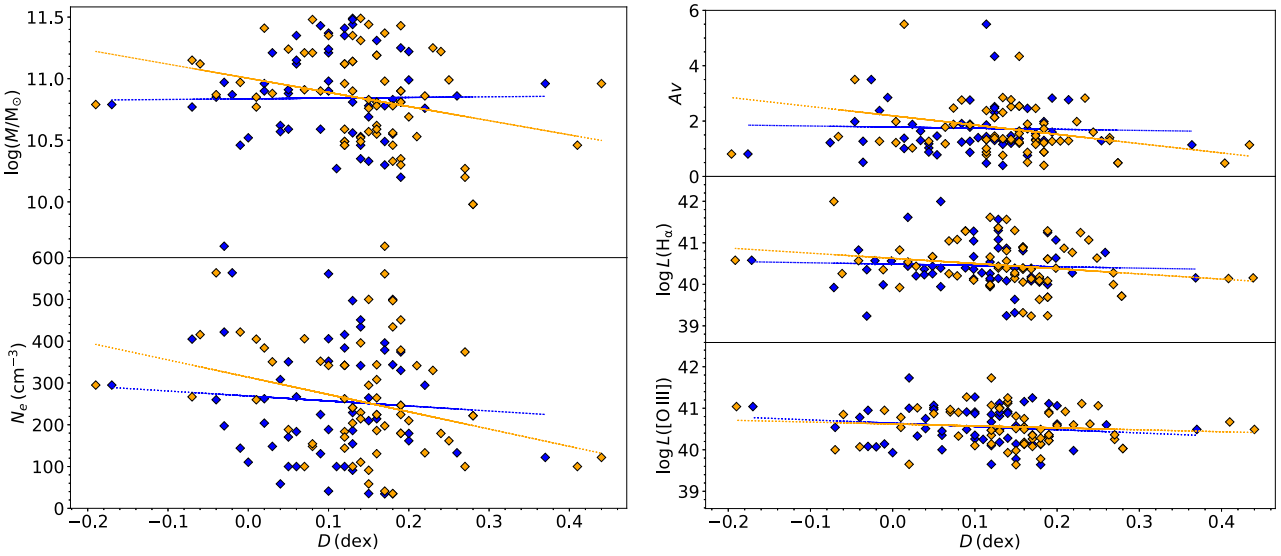

Figure 8. Left-hand panels: electron density (in units of cm^{-3}) for each AGN NLR and the logarithm of the stellar mass of the hosting galaxy versus the difference D (in dex, equation 12) between the O/H abundance of the AGN (derived from Carvalho et al. 2020 calibration – equation 10) and the intersect oxygen abundances derived from the radial abundance gradients – blue symbols for the H II O3N2 calibration and orange symbols for the N2 calibration of PMC09. Right-hand panels: as in the left-hand panels but for the logarithm of the luminosity of [O III]λ5007 and H α as well as the extinction A_v (in units of magnitude) of the AGNs. Blue and orange lines represent a linear regression to the corresponding points. The linear regression coefficients as well as the Pearson correlation coefficients (R) and p-values for the blue points are listed in Table 2, while those for the orange points are listed in Table 3.

Table 2. Coefficients of the linear regression to the blue symbols (O3N2 H II regions' O/H calibration) shown in Fig. 8, the corresponding Pearson correlation coefficient (R), and the p-value.

	a	b	R	p
N_e (cm^{-3})	− 119 ± 194.1	268.8 ± 27.19	−0.08	0.54
log($M/M_\odot$)	0.05 ± 0.57	10.84 ± 0.08	−0.01	0.93
log$L$([O III])	− 0.79 ± 0.63	40.64 ± 0.09	−0.16.	0.22
log$L$(H α)	− 0.32 ± 0.83	40.49 ± 0.12	−0.05	0.70
A_v	− 0.40 ± 1.58	1.78 ± 0.22	−0.03	0.82

Table 3. Coefficients of the linear regression to the orange symbols (N2 H II regions' O/H calibration) shown in Fig. 8, the corresponding Pearson correlation coefficient (R), and the p-value.

	a	b	R	p
N_e (cm^{-3})	− 413.7 ± 161.2	313.8 ± 27.87	−0.32	0.01
log($M/M_\odot$)	− 1.15 ± 0.48	11 ± 0.08	−0.30	0.02
log$L$([O III])	− 0.47 ± 0.56	40.62 ± 0.10	−0.11.	0.41
log$L$(H α)	− 1.25 ± 0.71	40.63 ± 0.12	−0.22	0.09
A_v	− 3.35 ± 1.31	2.21 ± 0.23	−0.32	0.01

Some recent studies have pointed out that star formation inside AGN gas outflows (e.g. Gallagher et al. 2019) and/or supernova explosions in accretion discs can locally enrich the AGN and produce very high abundances, mainly in the broad-line regions (e.g. Wang et al. 2011; Moranchel-Basurto et al. 2021). But, in our case, we find low metallicity in the NLRs of the sample, and, therefore, the most likely process is that we are observing an accretion of poor metal gas rather than a higher star formation rate in the innermost disc H II regions.

In order to investigate if there is any correlation between the oxygen discrepancy D, derived by using equation (12), and relevant physical properties of the AGN sample, in Fig. 8, we plot the electron density of the AGN NLR, luminosity of H α and the extinction coefficient A_v obtained within the inner 2.5 arcsec versus D. In addition, the luminosity of [O III]λ5007 and stellar masses derived from SDSS-III data (Thomas et al. 2013) were also plotted versus D in the second column of Fig. 8. The blue and orange symbols represent which calibration was considered in the radial extrapolation: blue for the O3N2 calibration and orange for the N2 calibration of PMC09. A linear regression to the points in each plot of Fig. 8 was performed. The best-fitting coefficients, the Pearson correlation coefficient (R) and the p-value are listed in Tables 2 and 3. The O/H abundances in the AGNs were those obtained through Carvalho et al. (2020) because this calibration considers a wider range of nebular parameters than that of SB_1. Based on the linear fits, R and p-values and from the analysis of the plots in Fig. 8, we can state that for the O3N2 calibration (represented by blue symbols), there is no correlation between the AGN and galaxy properties and D. The p-value confirms that R is not significant (considering the level of significance as $p \leq 0.05$). On the other hand, for the N2 calibration (represented by orange symbols), there is evidence of a mild inverse correlation between the following properties and D: electron density, stellar mass, and extinction A_v. The cause of these inverse correlations is not clear.

It is worthwhile to stress again that, the oxygen abundance estimations via strong-line methods for H II regions and AGNs can differ from each other up to ∼0.8 dex (e.g. Kewley & Ellison 2008; Dors et al. 2020b). Thus, to confirm the non-existence of correlation between AGN nebular parameters and D found above, it is necessary to estimate the O/H gradients and AGN abundances based on direct estimations of the electron temperature, i.e. by using the T_e-method (the most reliable method), which is not possible considering the data in this paper.

4 SUMMARY

We derived the metallicities of MaNGA AGN NLRs (traced by the O/H abundance) and the radial gradients of oxygen abundance along the disc for 98 Seyfert 2 and 10 Seyfert 1 host galaxies using MaNGA-SDSS-IV data cubes. The metallicities of the AGNs and in the disc of H II regions were obtained using calibrations based on strong emission lines proposed in the literature. We derived for most galaxies clear O/H gradients, with the O/H abundance ratio decreasing as the galactocentric distance increases. This characteristic is commonly found in the disc of spiral galaxies, which suggests that most spiral galaxies are formed according to the inside-out scenario. The oxygen abundances derived through emission lines of the AGNs and based on two distinct calibrations are lower by an average value $\langle D \rangle$ of 0.16–0.30 dex (depending on the calibration assumed) than the extrapolated oxygen abundances to the central parts derived from the radial abundance gradients. We suggest that the difference $\langle D \rangle$ can be due to the accretion of metal-poor gas to the AGN host – probably via the capture of a gas-rich dwarf galaxy, which builds up a reservoir of molecular and/or neutral gas that will then feed the SMBH. This gas will then trigger the nuclear activity via its capture by the nuclear SMBH. We investigated correlations between D and the electron density (N_e), [O III]λ5007, and Hα luminosities, extinction coefficient (A_V) of the AGN as well as the stellar mass (M_*) of the hosting galaxy. We did not find any significant correlation between the aforementioned properties and D when the oxygen gradients are derived from O3N2 index. Otherwise, there is evidence of an inverse correlation between the D and N_e, M_*, and A_v when the N2 index is used. The origin of inconsistency observed here, probably, it is due to the use of different metallicity indicators to derive the radial gradients. To confirm the derived correlations, further investigation with oxygen radial gradients and AGN estimations based on direct determination of the electron temperature, i.e. by using the T_e-method, is required.

ACKNOWLEDGEMENTS

JCN and OLD thank Fundaçó de Amparo á Pesquisa do Estado de São Paulo (FAPESP, process: 2019/14050-6). RR thanks Conselho Nacional de Desenvolvimento Científico e Tecnológico (CNPq, Proj. 311223/2020-6, 304927/2017-1, and 400352/2016-8), Fundação de amparo 'a pesquisa do Rio Grande do Sul (FAPERGS, Proj. 16/2551-0000251-7 and 19/1750-2), and Coordenação de Aperfeiçoamento de Pessoal de Nível Superior (CAPES, Proj. 0001). RAR thanks CNPq for partial financial support. TSB and SR acknowledge the support of the Brazilian funding agencies FAPERGS and CNPq. We would like to thank the support of the Instituto Nacional de Ciência e Tecnologia (INCT) e-Universe project

Funding for the Sloan Digital Sky Survey IV has been provided by the Alfred P. Sloan Foundation, the US Department of Energy Office of Science, and the Participating Institutions. SDSS acknowledges support and resources from the Center for High-Performance Computing at the University of Utah. The SDSS website is www.sdss.org.

SDSS is managed by the Astrophysical Research Consortium for the Participating Institutions of the SDSS Collaboration including the Brazilian Participation Group, the Carnegie Institution for Science, Carnegie Mellon University, the Chilean Participation Group, the French Participation Group, Harvard-Smithsonian Center for Astrophysics, Instituto de Astrofísica de Canarias, The Johns Hopkins University, Kavli Institute for the Physics and Mathematics of the Universe (IPMU)/University of Tokyo, Lawrence Berkeley National Laboratory, Leibniz Institut für Astrophysik Potsdam (AIP), Max-Planck-Institut für Astronomie (MPIA Heidelberg), Max-Planck-Institut für Astrophysik (MPA Garching), Max-Planck-Institut für Extraterrestrische Physik (MPE), National Astronomical Observatories of China, New Mexico State University, New York University, University of Notre Dame, Observatório Nacional/MCTI, The Ohio State University, Pennsylvania State University, Shanghai Astronomical Observatory, United Kingdom Participation Group, Universidad Nacional Autónoma de México, University of Arizona, University of Colorado Boulder, University of Oxford, University of Portsmouth, University of Utah, University of Virginia, University of Washington, University of Wisconsin, Vanderbilt University, and Yale University.

DATA AVAILABILITY

The data underlying this paper are available under SDSS collaboration rules, and the by-products will be shared on reasonable request to the corresponding author.

REFERENCES

Aguado D. S. et al., 2019, ApJS, 240, 23
Alende Prieto C., Lambert D. L., Asplund M., 2001, ApJ, 556, L63
Allen M. G., Groves B. A., Dopita M. A., Sutherland R. S., Kewley L. J., 2008, ApJS, 178, 20
Allen J. T. et al., 2015, MNRAS, 451, 2780
Allison J. R. et al., 2015, MNRAS, 453, 1249
Alloin D., Collin-Souffrin S., Joly M., Vigroux L., 1979, A&A, 78, 200
Baldwin J. A., Phillips M. M., Terlevich R., 1981, PASP, 93, 5
Belfiore F. et al., 2017, MNRAS, 469, 151
Berg D. A., Skillman E. D., Croxall K. V., Pogge R. W., Moustakas J., Johnson-Groh M., 2015, ApJ, 806, 16
Berg D. A., Pogge R. W., Skillman E. D., Croxall K. V., Moustakas J., Rogers Noah S. J., Sun J., 2020, ApJ, 893, 96
Blanton M. R. et al., 2017, AJ, 154, 28
Bundy K. et al., 2015, ApJ, 798, 7
Buzzo M. L. et al., 2021, MNRAS, 503, 106
Carvalho S. P. et al., 2020, MNRAS, 492, 5675
Castro C. S., Dors O. L., Cardaci M. V., Hägele G. F., 2017, MNRAS, 467, 1507
Cid Fernandes R., Stasińska G., Schlickmann M. S., Mateus A., Vale Asari N., Schoenell W., Sodrhoenell W., Sodré L., 2010, MNRAS, 403, 1036
Comerford J. M., Greene J. E., 2014, ApJ, 789, 112
Congiu E. et al., 2017, MNRAS, 471, 562
Copetti M. V. F., Mallmann J. A. H., Schmidt A. A., Castañeda H. O., 2000, A&A, 357, 621
Cresci G., Mannucci F., Maiolino R., Marconi A., Gnerucci A., Magrini L., 2010, Nature, 467, 811
Croom S. M. et al., 2012, MNRAS, 421, 872
Croxall K. V., Pogge R. W., Berg D. A., Skillman E. D., Moustakas J., 2015, ApJ, 808, 42
Croxall K. V., Pogge R. W., Berg D. A., Skillman E. D., Moustakas J., 2016, ApJ, 830, 4
Davies R. et al., 2020, MNRAS, 498, 4150
Davies R. L., Kewley L. S., Ho I-T., Dopita M., 2014, MNRAS, 444, 3961
Denicoló G., Terlevich R., Terlevich E., 2002, MNRAS, 330, 69 (DTT02)
do Nascimento J. C. et al., 2019, MNRAS, 486, 5075
Dors O. L., 2021, MNRAS, 507, 466
Dors O. L., Copetti M. V. F., 2005, A&A, 437, 837
Dors O. L., Cardaci M. V., Hägele G. F., Krabbe Â. C., 2014, MNRAS, 443, 1291
Dors O. L., Cardaci M. V., Hägele G. F., Rodrigues I., Grebel E. K., Pilyugin L. S., Freitas-Lemes P., Krabbe A. C., 2015, MNRAS, 453, 4102
Dors O. L., Häagele G. F., Cardaci M. V., Krabbe A. C., 2017, MNRAS, 466, 726
Dors O. L., Agarwal B., Hägele G. F., Cardaci M. V., Rydberg C., Riffel R. A., Oliveira A. S., Krabbe A. C., 2018, MNRAS, 479, 2294

Dors O. L., Monteiro A. F, Cardaci M. V., Hägele G. F., Krabbe Â. C., 2019, MNRAS, 486, 5853
Dors O. L. et al., 2020a, MNRAS, 492, 468
Dors O. L., Maiolino R., Cardaci M. V., Hagele G. F., Krabbe A. C., Perez-Montero E. A. M., 2020b, MNRAS, 496, 3209
Dors O. L., Contini M., Riffel R. A., Pérez-Montero E., Krabbe A. C., Cardaci M. V., Hägele G. F., 2021, MNRAS, 501, 1370
Drory N. et al., 2015, AJ, 149, 77
Esteban C., Peimbert M., Torres-Peimbert S., Escalante V., 1998, MNRAS, 295, 401
Feltre A., Charlot S., Gutkin J., 2016, MNRAS, 456, 3354
Ferland G. J., 2017, Rev. Mex. Astron. Astrofis., 53, 385
Ferland G. J., Netzer H., 1983, ApJ, 264, 105
Ferland G. J., Osterbrock D. E., 1986, ApJ, 300, 658
Flury S. R., Moran E. C., 2020, MNRAS, 496, 2191
Freitas I. C. et al., 2018, MNRAS, 476, 2760
Gallagher R., Maiolino R., Belfiore F., Drory N., Riffel R., Riffel R. A., 2019, MNRAS, 485, 3409
Gillman S. et al., 2021, MNRAS, 500, 4229
Groves B. A., Heckman T. M., Kauffmann G., 2006, MNRAS, 371, 1559
Gunn J. E. et al., 2006, AJ, 131, 2332
Guo Y. et al., 2020, ApJ, 898, 26
Hagele G. F., Diaz A. I., Terlevich E., Terlevich R., Perez-Montero E., Cardaci M. V., 2008, MNRAS, 383, 209
Hampton E. J. et al., 2017, MNRAS, 470, 3395
Ho L. C., Filippenko A. V., Sargent W. L. W., 1997, ApJS, 112, 315
Ilha G. S. et al., 2019, MNRAS, 484, 252
Izotov Y. I., Stasinska G., Meynet G., Guseva N. G., Thuan T. X., 2006, A&A, 448, 955
Jenkins E. B., 2009, ApJ, 700, 1299
Ji X., Yan R., Riffel R., Drory N., Zhang K., 2020, MNRAS, 496, 1262
Kakkad D. et al., 2018, A&A, 618, A6
Kaplan K. F. et al., 2016, MNRAS, 462, 1642
Kauffmann G. et al., 2003, MNRAS, 346, 1055
Kennicutt R. C., Bresolin F., Garnett D. R., 2003, ApJ, 591, 801
Kewley L. J., Ellison S. L., 2008, ApJ, 681, 1183
Kewley L. J., Dopita M. A., Sutherland R. S., Heisler C. A., Trevena J., 2001, ApJ, 556, 121
Kewley L. J., Groves B., Kauffmann G., Heckman T., 2006, MNRAS, 372, 961
Krabbe A. C., Rosa D. A., Dors O. L., Pastoriza M. G., Winge C., Hagele G. F., Cardaci M. V., Rodrigues I., 2014, MNRAS, 437, 1155
Krabbe A. C., Oliveira C. B., Zinchenko I. A., Hernández-Jiménez J. A., Dors O. L., Hägele G. F., Cardaci M. V., Telles N. R., 2021, MNRAS, 505, 2087
Kumari N., James B. L., Irwin M. J., 2017, MNRAS, 470, 4618
Kumari N., Maiolino R., Belfiore F., Curti M., 2019, MNRAS, 485, 367
Law D. R. et al., 2015, AJ, 150, 19
Law D. R. et al., 2016, AJ, 152, 83
Lòpez-Sìchez A. R., Dopita M. A., Kewley L. J., Zahid H. J., Nicholls D. C., Scharwachter J., 2012, MNRAS, 426, 2630
Marino R. A. et al., 2013, A&A, 559, A114
Matsuoka K., Nagao T., Maiolino R., Marconi A., Taniguchi Y., 2009, A&A, 503, 721
Matsuoka K., Nagao T., Marconi A., Maiolino R., Mannucci F., Cresci G., Terao K., Ikeda H., 2018, A&A, 616, L4
Meyer D. M., Jura M., Cardelli J. A., 1998, ApJ, 493, 222
Mignoli M. et al., 2019, A&A, 626, 9
Mingozzi M. et al., 2019, A&A, 622A, 146
Mingozzi M. et al., 2020, A&A, 636, A42
Moiré H. G., Rogemar R. A., Dors O. L., Riffel R., Storchi-Bergmann T., Colina L., 2018, MNRAS, 477, 1086
Mollá M., Díaz A. I., 2005, MNRAS, 358, 521
Mora M. D., Torres-Flores S., Firpo V., Hernandez-Jimenez J. A., Urrutia-Viscarra F., Mendes de Oliveira C., 2019, MNRAS, 488, 830
Moranchel-Basurto A., Sánchez-Salcedo F. J. , Chametla R. O., Velázquez P. F., 2021, ApJ, 906, 15
Nagao T., Maiolino R., Marconi A., 2006, A&A, 447, 863
Nakajima K. et al., 2018, A&A, 612, 94
Pagel B. E. J., Edmunds M. G., Blackwell D. E., Chun M. S., Smith G., 1979, MNRAS, 189, 95
Paulino-Afonso A. et al., 2019, A&A, 630, A57
Peimbert M., Peimbert A., Delgado-Inglada G., 2017, PASP, 129, 2001
Peña-Guerrero M. A., Peimbert A., Peimbert M., 2012, ApJ, 756, L14
Pérez-Montero E., 2017, PASP, 129, 3001
Pérez-Montero E., Contini T., 2009, MNRAS, 398, 949 (PMC09)
Pérez-Montero E., Dors O. L., Vílchez J. M., García-Benito R., Cardaci M. V., Hägele G. F., 2019, MNRAS, 489, 2652
Pettini M., Pagel B. E. J., 2004, MNRAS, 348, L59 (PP04)
Pilyugin L. S., 2000, A&A, 362, 325
Pilyugin L. S., 2001, A&A, 369, 594
Pilyugin L. S., Vílchez J. M., Contini T., 2004, A&A, 425, 849
Pilyugin L. S., Grebel E. K., Mattsson L., 2012, MNRAS, 424, 2316
Pilyugin L. S., Lara-López M. A., Grebel E. K., Kehrig C., Zinchenko I. A., López-Sánchez A. R., Vílchez J. M., Mattsson L., 2013, MNRAS, 432, 1217
Rembold S. B. et al., 2017, MNRAS, 472, 4382
Revalski M., Crenshaw D. M., Kraemer S. B., Fischer T. C., Schmitt H. R., Machuca C., 2018, ApJ, 856, 46
Riffel R. A., Storchi-Bergmann T., Winge C., McGregor P. J., Beck T., Schmitt H., 2008, MNRAS, 385, 1129
Riffel R. A., Storchi-Bergmann T., Winge C., 2013, MNRAS, 430, 2249
Riffel R. et al., 2021, MNRAS, 501, 4064
Rogers N. S. J., Skillman E D., Pogge R. W., Berg D. A., Moustakas J., Croxall K. V., Sun J., 2021, ApJ, 915, 21
Rosa D. A., Dors O. L., Krabbe A. C., Hagele G. F., Cardaci M. V., Pastoriza M. G., Rodrigues I., Winge C., 2014, MNRAS, 444, 2005
Rosa D. A., Rodrigues I., Krabbe A. C., Milone A. C., Carvalho S., 2021, MNRAS, 501, 3750
Sánchez S. F. et al., 2014, A&A, 563, 49
Sánchez S. F. et al., 2012, A&A, 538, A8
Sarzi M. et al., 2006, MNRAS, 366, 1151
Shaver P. A., McGee R. X., Newton L. M., Danks A. C., Pottasch S. R., 1983, MNRAS, 204, 53
Simons R. C. et al., 2020, ApJ, 923, 203
Skillman E. D., Kennicutt R. C., 1993, ApJ, 411, 655
Skillman E. D., Berg D. A., Pogge R. W., Moustakas J., Rogers N. S. J., Croxall K. V., 2020, ApJ, 894, 138
Smee S. A. et al., 2013, AJ, 146, 32
Somerville R. S., Davé R., 2015, ARA&A, 53, 51
Stasińska G., 1984, A&A, 135, 341
Sternberg A., Genzel R., Tacconi L., 1994, ApJ, 436, L131
Storchi-Bergmann T., Calzetti D., Kinney A. L., 1994, ApJ, 429, 572
Storchi-Bergmann T., Schmitt H. R., Calzetti D., Kinney A. L., 1998, AJ, 115, 909 (SB1)
Storchi-Bergmann T., Dors O. L., Riffel R. A., Fathi K., Axon D. J., Robinson A., Marconi A., Östlin G., 2007, ApJ, 670, 959
Storchi-Bergmann T., Schnorr-Müller A., 2019, Nat. Astron., 3, 48
Thomas D. et al., 2013, MNRAS, 431, 1383
Usero A., García-Burillo S., Fuente A., Martín-Pintado J., Rodríguez-Fernández N. J., 2004, A&A, 419, 897
van Zee L., Salver J. J., Haynes M. P., O'Donoghe A. A., Balonek T. J., 1998, AJ, 116, 2805
Vaona L., Ciroi S., Di Mille F., Cracco V., La Mura G., Rafanelli P., 2012, MNRAS, 427, 1266
Wake D. A. et al., 2017, AJ, 154, 86
Wang J.-M. et al., 2011, ApJ, 739, 3
Werk J. K., Putman M. E., Meurer G. R., Thilker D. A., Allen R. J., Bland-Hawthorn J., Kravtsov A., Freeman K., 2010, ApJ, 715, 656
Whittet D. C. B., 2010, ApJ, 710, 1009
Wright E. L., 2006, PASP, 118, 1711
Wu H., Zhu Y.-N., Cao C., Qin B., 2007, ApJ, 668, 87
Wu Y.-Z., 2020, ApJ, 893, L33
Wu Y.-Z., 2021, ApJS, 252, 8
Yan R. et al., 2016, AJ, 152, 197

Yates R. M., Kauffmann G., Guo Q., 2012, MNRAS, 422, 215
York D. G., et al., 2000, AJ, 120, 1579
Zhang Z. T., Liang Y. C., Hammer F., 2013, MNRAS, 430, 2605
Zinchenko I. A., Dors O. L., Hagele G. F., Cardaci V. F., Krabbe A. C., 2019, MNRAS, 483, 1901

SUPPORTING INFORMATION

Supplementary data are available at *MNRAS* online.

Figure S1. As Fig. 3 but for the AGN host 1-44303.
Figure S2. As Fig. 3 but for the AGN host 1-460812.
Figure S3. As Fig. 3 but for the AGN host 1-24148.
Figure S4. As Fig. 3 but for the AGN host 1-163966.
Figure S5. As Fig. 3 but for the AGN host 1-149561.
Figure S6. As Fig. 3 but for the AGN host 1-24660.
Figure S7. As Fig. 3 but for the AGN host 1-258373.
Figure S8. As Fig. 3 but for the AGN host 1-296733.
Figure S9. As Fig. 3 but for the AGN host 1-60653.
Figure S10. As Fig. 3 but for the AGN host 1-109056.
Figure S11. As Fig. 3 but for the AGN host 1-210646.
Figure S12. As Fig. 3 but for the AGN host 1-248420.
Figure S13. As Fig. 3 but for the AGN host 1-277552.
Figure S14. As Fig. 3 but for the AGN host 1-96075.
Figure S15. As Fig. 3 but for the AGN host 1-269632.
Figure S16. As Fig. 3 but for the AGN host 1-209980.
Figure S17. As Fig. 3 but for the AGN host 1-44379.
Figure S18. As Fig. 3 but for the AGN host 1-279147.
Figure S19. As Fig. 3 but for the AGN host 1-94784.
Figure S20. As Fig. 3 but for the AGN host 1-137883.
Figure S21. As Fig. 3 but for the AGN host 1-48116.
Figure S22. As Fig. 3 but for the AGN host 1-135641.
Figure S23. As Fig. 3 but for the AGN host 1-248389.
Figure S24. As Fig. 3 but for the AGN host 1-321739.
Figure S25. As Fig. 3 but for the AGN host 1-234618.
Figure S26. As Fig. 3 but for the AGN host 1-542318.
Figure S27. As Fig. 3 but for the AGN host 1-279676.
Figure S28. As Fig. 3 but for the AGN host 1-519742.
Figure S29. As Fig. 3 but for the AGN host 1-94604.
Figure S30. As Fig. 3 but for the AGN host 1-148068.
Figure S31. As Fig. 3 but for the AGN host 1-603941.
Figure S32. As Fig. 3 but for the AGN host 1-153627.
Figure S33. As Fig. 3 but for the AGN host 1-270129.
Figure S34. As Fig. 3 but for the AGN host 1-298938.
Figure S35. As Fig. 3 but for the AGN host 1-420924.
Figure S36. As Fig. 3 but for the AGN host 1-626658.
Figure S37. As Fig. 3 but for the AGN host 1-603039.
Figure S38. As Fig. 3 but for the AGN host 1-43868.
Figure S39. As Fig. 3 but for the AGN host 1-174631.
Figure S40. As Fig. 3 but for the AGN host 1-617323.
Figure S41. As Fig. 3 but for the AGN host 1-176644.
Figure S42. As Fig. 3 but for the AGN host 1-179679.
Figure S43. As Fig. 3 but for the AGN host 1-196597.
Figure S44. As Fig. 3 but for the AGN host 1-210020.
Figure S45. As Fig. 3 but for the AGN host 1-633942.
Figure S46. As Fig. 3 but for the AGN host 1-277257.
Figure S47. As Fig. 3 but for the AGN host 1-298778.
Figure S48. As Fig. 3 but for the AGN host 1-299013.
Figure S49. As Fig. 3 but for the AGN host 1-323794.
Figure S50. As Fig. 3 but for the AGN host 1-405760.
Figure S51. As Fig. 3 but for the AGN host 1-625513.
Figure S52. As Fig. 3 but for the AGN host 1-547402.
Figure S53. As Fig. 3 but for the AGN host 1-175889.
Figure S54. As Fig. 3 but for the AGN host 1-605353.
Figure S55. As Fig. 3 but for the AGN host 1-232143.
Figure S56. As Fig. 3 but for the AGN host 1-251458.
Figure S57. As Fig. 3 but for the AGN host 1-298298.
Figure S58. As Fig. 3 but for the AGN host 1-380097.
Figure S59. As Fig. 3 but for the AGN host 1-31788.
Figure S60. As Fig. 3 but for the AGN host 1-150947
Figure S61. As Fig. 3 but for the AGN host 1-604912.
Figure S62. As Fig. 3 but for the AGN host 1-145679
Figure S63. As Fig. 3 but for the AGN host 1-163789.
Figure S64. As Fig. 3 but for the AGN host 1-153901.
Figure S65. As Fig. 3 but for the AGN host 1-201969.
Figure S66. As Fig. 3 but for the AGN host 1-229862.
Figure S67. As Fig. 3 but for the AGN host 1-229731.
Figure S68. As Fig. 3 but for the AGN host 1-264729.
Figure S69. As Fig. 3 but for the AGN host 1-268479.
Figure S70. As Fig. 3 but for the AGN host 1-295041.
Figure S71. As Fig. 3 but for the AGN host 1-281125.
Figure S72. As Fig. 3 but for the AGN host 1-382697.
Figure S73. As Fig. 3 but for the AGN host 1-403982.
Figure S74. As Fig. 3 but for the AGN host 1-605215.
Figure S75. As Fig. 3 but for the AGN host 1-457424.

Please note: Oxford University Press is not responsible for the content or functionality of any supporting materials supplied by the authors. Any queries (other than missing material) should be directed to the corresponding author for the article.

This paper has been typeset from a TEX/LATEX file prepared by the author.